

PREPARED FOR SUBMISSION TO JHEP

Amplitude analysis and branching fraction measurement of the decay $D^+ \rightarrow K_S^0 \pi^+ \pi^0 \pi^0$

The BESIII Collaboration



ABSTRACT: Using 2.93 fb^{-1} of e^+e^- collision data collected with the BESIII detector at the center-of-mass energy 3.773 GeV , we perform the first amplitude analysis of the decay $D^+ \rightarrow K_S^0 \pi^+ \pi^0 \pi^0$ and determine the relative magnitudes and phases of different intermediate processes. The absolute branching fraction of $D^+ \rightarrow K_S^0 \pi^+ \pi^0 \pi^0$ is measured to be $(2.888 \pm 0.058_{\text{stat.}} \pm 0.069_{\text{syst.}})\%$. The dominant intermediate processes are $D^+ \rightarrow K_S^0 a_1(1260)^+ (\rightarrow \rho^+ \pi^0)$ and $D^+ \rightarrow \bar{K}^{*0} \rho^+$, with branching fractions of $(8.66 \pm 1.04_{\text{stat.}} \pm 1.39_{\text{syst.}}) \times 10^{-3}$ and $(9.70 \pm 0.81_{\text{stat.}} \pm 0.53_{\text{syst.}}) \times 10^{-3}$, respectively.

KEYWORDS: Charm Physics, e^+e^- Experiments, Particle and Resonance Production, Branching fraction

Contents

1	Introduction	1
2	Detector and data sets	2
3	Event selection	3
4	Amplitude analysis	4
4.1	Further selection criteria	4
4.2	Fit method	4
4.2.1	Blatt-Weisskopf barriers	7
4.2.2	Propagator	8
4.2.3	Spin factors	10
4.3	Fit results	11
4.4	Systematic uncertainties for the amplitude analysis	12
5	BF measurement	14
6	Summary	19
A	Two-dimensional fit on $M_{\text{BC}}^{\text{sig}}$ versus $M_{\text{BC}}^{\text{tag}}$	22
B	Other tested intermediate processes	24
C	The interference between processes	25

1 Introduction

Hadrons containing a charm quark play an essential role in studies of the strong and weak interactions. The lightest charmed mesons, $D^{0(+)}$, can decay only through the weak interaction and their masses place them in the region where perturbative Quantum Chromodynamics is not applicable [1]. These facts do not significantly affect the theoretical prediction of leptonic and semileptonic decays but impose difficulties in hadronic decays [2]. Measurements of amplitudes and branching fractions (BFs) of charmed meson hadronic decays could provide useful information about the underlying decay mechanism and help to improve theoretical calculations.

The Cabibbo-favored decay $D^+ \rightarrow K_S^0 \pi^+ \pi^0 \pi^0$ has been previously observed by BESIII with a BF of $(2.904 \pm 0.062_{\text{stat.}} \pm 0.087_{\text{syst.}})\%$ [3]. However, the corresponding detector efficiency was obtained by mixed-signal Monte Carlo (MC) samples, which can now be improved by using an amplitude model. An amplitude analysis of this four-body decay,

compared to well-measured three-body decays [4–6], can also help us better understand the more complicated dynamics and substructures in the processes $D^+ \rightarrow VV$ and $D^+ \rightarrow AP$, where V , A , and P denote vector, axial-vector and pseudoscalar mesons, respectively. The BF of $D^+ \rightarrow \bar{K}^{*0}\rho^+$, which is a Cabibbo-favored $D^+ \rightarrow VV$ process, can be measured more precisely in comparison to the previous MARK III result [7]. An amplitude analysis can provide inputs for polarization studies to check the reliability of different theoretical models [8]. Furthermore, measurements of $D^+ \rightarrow AP$ decays are beneficial for our understanding of the nature of axial-vector mesons and offer global parameters in calculating the corresponding BFs [9]. The difference between the production rates of $K_1(1270)$ and $K_1(1400)$ can be extracted, which provide key inputs to determine the mixing between these two mesons [10].

With 2.93 fb^{-1} of e^+e^- collision data collected by the BESIII detector at the center-of-mass energy $\sqrt{s} = 3.773 \text{ GeV}$, we present the first amplitude analysis of the decay $D^+ \rightarrow K_S^0\pi^+\pi^0\pi^0$ and update the BF based on the corresponding amplitude model. The daughter particle K_S^0 is reconstructed by $\pi^+\pi^-$. Charge-conjugate states are implied throughout this paper.

2 Detector and data sets

The BESIII detector is a magnetic spectrometer [11, 12] located at the Beijing Electron Positron Collider (BEPCII) [13], which records symmetric e^+e^- collisions in the center-of-mass energy range from 2.0 to 4.95 GeV, with a peak luminosity of $1 \times 10^{33} \text{ cm}^{-2}\text{s}^{-1}$ achieved at $\sqrt{s} = 3.77 \text{ GeV}$. The cylindrical core of the BESIII detector covers 93% of the full solid angle and consists of a helium-based multilayer drift chamber (MDC), a plastic scintillator time-of-flight system (TOF), and a CsI(Tl) electromagnetic calorimeter (EMC), which are all enclosed in a superconducting solenoidal magnet providing a 1.0 T magnetic field. The solenoid is supported by an octagonal flux-return yoke with resistive plate counter muon identifier modules interleaved with steel. The charged-particle momentum resolution at 1.0 GeV/c is 0.5%, and the specific ionization energy loss (dE/dx) resolution is 6% for the electrons from Bhabha scattering. The EMC measures photon energies with a resolution of 2.5% (5%) at 1 GeV in the barrel (end-cap) region. The time resolution in the TOF barrel region is 68 ps, while that in the end-cap region is 110 ps.

Data samples corresponding to a total integrated luminosity of 2.93 fb^{-1} at $\sqrt{s} = 3.773 \text{ GeV}$ are used in this analysis. This energy is slightly higher than the resonance peak of the $\psi(3770)$, which predominantly decays to D^+D^- or $D^0\bar{D}^0$ pairs without any additional hadrons, thereby providing an ideal environment for studying D meson decays with the double-tag (DT) technique [14]. In this method, a single-tag (ST) candidate requires only one D^- to be reconstructed via hadronic decays. In a DT candidate, both the D^+ and D^- mesons are reconstructed, with the D^+ meson decaying to the signal mode $D^+ \rightarrow K_S^0\pi^+\pi^0\pi^0$ and the D^- meson decaying to one of the ST modes.

Simulated inclusive MC samples are produced with a GEANT4-based [15] MC simulation package, which includes the geometric description of the BESIII detector [16] and the detector response, and are used to determine detection efficiencies and to estimate back-

grounds. The simulation models the beam energy spread and initial state radiation (ISR) in the e^+e^- annihilations with the generator KKMC [17, 18]. The inclusive MC samples consist of the production of $D\bar{D}$ pairs, the non- $D\bar{D}$ decays of the $\psi(3770)$, the ISR production of the J/ψ and $\psi(3686)$ states, and the continuum processes incorporated in KKMC. All particle decays are modelled with EVTGEN [19, 20] using BFs either taken from the Particle Data Group (PDG) [21], when available, or otherwise estimated with LUNDCHARM [22, 23]. Final state radiation from charged final state particles is incorporated using PHOTOS [24].

3 Event selection

The D^\pm candidates are constructed from individual π^\pm , π^0 , K^\pm , and K_S^0 mesons with the following selection criteria, which are the common requirements for both the amplitude analysis and BF measurement. Further requirements are discussed in Sec. 4.1 and Sec. 5, respectively.

All charged tracks detected in the MDC must satisfy $|\cos\theta| < 0.93$, where θ is defined as the polar angle with respect to the z -axis, which is the symmetry axis of the MDC. For charged tracks not originating from K_S^0 decays, the distance of closest approach to the interaction point (IP) is required to be less than 10 cm along the z -axis, $|V_z|$, and less than 1 cm in the transverse plane, $|V_{xy}|$. Particle identification (PID) for charged tracks combines the measurements of the dE/dx in the MDC and the flight time in the TOF to form probabilities $\mathcal{L}(h)$ ($h = K, \pi$) for each hadron (h) hypothesis. The charged kaons and pions are identified by comparing the likelihoods for the kaon and pion hypotheses, $\mathcal{L}(K) > \mathcal{L}(\pi)$ and $\mathcal{L}(\pi) > \mathcal{L}(K)$, respectively.

Each K_S^0 candidate is reconstructed from two oppositely charged tracks satisfying $|V_z| < 20$ cm. The two charged tracks are assigned as $\pi^+\pi^-$ without imposing PID. They are constrained to originate from a common vertex and are required to have an invariant mass within $|M_{\pi^+\pi^-} - m_{K_S^0}| < 12$ MeV/ c^2 , where $m_{K_S^0}$ is the known K^0 mass [21]. The decay length of the K_S^0 candidate is required to be greater than twice its resolution.

Photon candidates are selected using the EMC showers. The deposited energy of each shower in the barrel region ($|\cos\theta| < 0.80$) and in the end-cap region ($0.86 < |\cos\theta| < 0.92$) must be greater than 25 MeV and 50 MeV, respectively. To exclude showers that originate from charged tracks, the angle subtended by the EMC shower and the position of the closest charged track at the EMC must be greater than 10 degrees as measured from the interaction point. The difference between the EMC time and the event start time is required to be within [0, 700] ns to suppress electronic noise and showers unrelated to the event.

The π^0 candidates are reconstructed from photon pairs with invariant masses in the range [0.115, 0.150] GeV/ c^2 , which corresponds to about three times the standard deviation of the invariant mass resolution. We require that at least one photon comes from the barrel region of the EMC to improve the resolution. Furthermore, the π^0 candidates are constrained to the known π^0 mass [21] via a kinematic fit to improve their energy and momentum resolution.

Two variables, the beam-constrained mass M_{BC} and the energy difference ΔE , are used to identify the D^\pm mesons:

$$\begin{aligned} M_{\text{BC}} &= \sqrt{E_{\text{beam}}^2/c^4 - |\vec{p}_{D^\pm}|^2/c^2}, \\ \Delta E &= E_{D^\pm} - E_{\text{beam}}, \end{aligned} \quad (3.1)$$

where E_{beam} is the calibrated beam energy, and \vec{p}_{D^\pm} and E_{D^\pm} are the total reconstructed momentum and energy of the D^\pm candidate, respectively. The D^\pm signals will appear as a peak at the known D^\pm mass [21] in the M_{BC} distribution and as a peak at zero in the ΔE distribution. If multiple DT candidates exist in one event, the candidate with the minimum quadratic sum of ΔE from the two D^\pm mesons ($\Delta E_{\text{tag}}^2 + \Delta E_{\text{sig}}^2$) is retained.

4 Amplitude analysis

4.1 Further selection criteria

To increase the signal purity for amplitude analysis, only one ST mode $D^- \rightarrow K^+ \pi^- \pi^-$ is used due to its high statistics and low background level. We require that $\Delta E \in [-0.025, 0.020]$ ($[-0.040, 0.020]$) GeV must be satisfied for the tag (signal) side. The following dedicated selection criteria are imposed on the signal candidates and will not be used in the BF measurement.

A K_S^0 mass veto, $M_{\pi^0\pi^0} \notin [0.46, 0.52]$ GeV/ c^2 , is used to suppress the dominant background from $D^+ \rightarrow K_S^0 K_S^0 \pi^+$ in which one of the two K_S^0 mesons decays to $\pi^0\pi^0$. Another source of background comes from the process $D^0 \rightarrow K_S^0 \pi^+ \pi^- \pi^0$ versus $\bar{D}^0 \rightarrow K^+ \pi^- \pi^0$, which can be miscombined to fake the signal process $D^+ \rightarrow K_S^0 \pi^+ \pi^0 \pi^0$ versus $D^- \rightarrow K^+ \pi^- \pi^-$ by exchanging the π^- from D^0 decay and the π^0 from \bar{D}^0 decay. We reconstruct this background and calculate the wrong beam-constrained mass M_{BC}^W and the wrong energy difference ΔE^W according to the $D^0 \bar{D}^0$ decay mode. For multiple miscombined candidates, we use the minimum quadratic sum of ΔE^W to select the “best background” event. Figure 1 shows the M_{BC}^W distribution for this background and the signal process from MC simulation. The background will form a peak at the known D^0 mass [21] while the distribution for signal is flat. Therefore, it is excluded by rejecting events which simultaneously satisfy $1.862 < M_{\text{BC}}^W < 1.870$ GeV/ c^2 for both the tag and the signal sides.

We perform a four-constraint kinematic fit to ensure that all events land within the phase space boundary. The invariant masses of the signal D^+ candidate, the K_S^0 , and the two π^0 s are constrained to the corresponding known masses [21]. The updated four-momenta of the final state particles from the kinematic fit are used to perform the amplitude analysis. After applying all selection criteria, we perform an unbinned two-dimensional (2D) maximum likelihood fit (see appendix A) to the distribution $M_{\text{BC}}^{\text{tag}}$ versus $M_{\text{BC}}^{\text{sig}}$ to estimate the signal purity, as shown in figure 2. There are 1,458 events remaining in the signal region for amplitude analysis with a purity of $(96.86 \pm 0.46)\%$.

4.2 Fit method

The amplitude analysis of $D^+ \rightarrow K_S^0 \pi^+ \pi^0 \pi^0$ is performed by an unbinned maximum likelihood fit. The likelihood function \mathcal{L} is constructed by adding the background probability

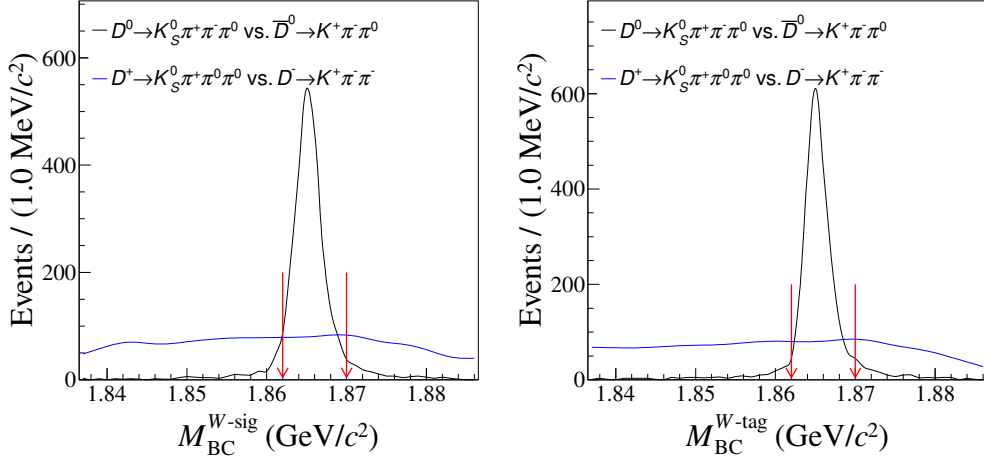


Figure 1. The M_{BC}^W distributions for miscombined background and the signal process from MC simulation. The left is for signal side, and the right is for tag side. The black and blue lines are miscombined background and the signal process, respectively. The pairs of red arrows indicate the related veto region.

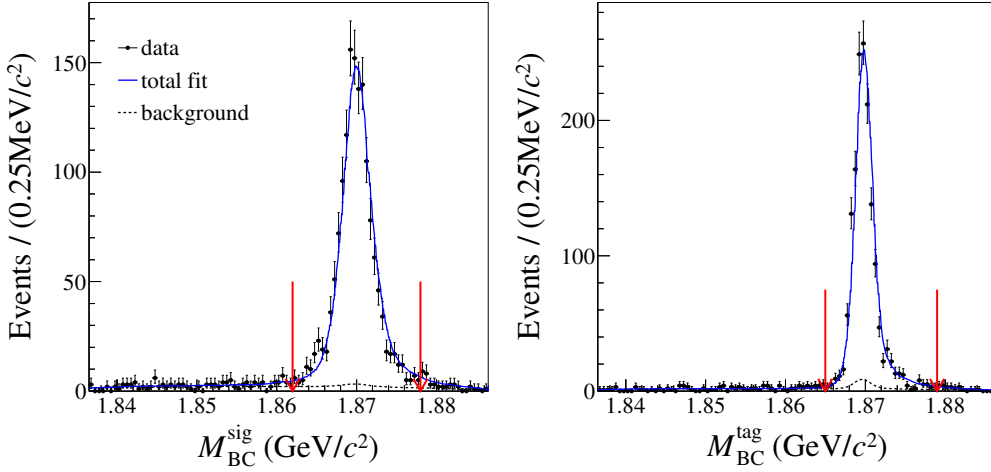


Figure 2. The projections of the 2D fit on $M_{\text{BC}}^{\text{sig}}$ (left) versus $M_{\text{BC}}^{\text{tag}}$ (right). The black points with error bars are data. The blue solid and black dashed lines are the total fits and the backgrounds, respectively. The pairs of red arrows indicate the signal region, $[1.862, 1.878]$ GeV/c^2 for the signal side and $[1.865, 1.879]$ GeV/c^2 for the tag side.

density function (PDF) to the signal PDF incoherently. After taking the logarithm, the combined PDF can be written as

$$\ln \mathcal{L} = \sum_k^{N_{\text{data}}} \ln [\omega_{\text{sig}} f_S(p_j^k) + (1 - \omega_{\text{sig}}) f_B(p_j^k)], \quad (4.1)$$

where k indicates the k^{th} event in the data sample, N_{data} is the number of surviving events, p_j denotes the four-momenta of the j^{th} final state particles, $f_S(f_B)$ is the signal (background) PDF and ω_{sig} is the signal purity discussed in Sec. 4.1.

The signal PDF is given by

$$f_S(p_j) = \frac{\epsilon(p_j)|\mathcal{M}(p_j)|^2 R_4(p_j)}{\int \epsilon(p_j)|\mathcal{M}(p_j)|^2 R_4(p_j) dp_j}, \quad (4.2)$$

where $\epsilon(p)$ is the detection efficiency and $R_4(p)$ is the four-body phase space. The total amplitude \mathcal{M} is treated within the isobar model, which uses the coherent sum of amplitudes of intermediate processes, given by $\mathcal{M}(p) = \sum c_n \mathcal{A}_n(p)$, where $c_n = \rho_n e^{i\phi_n}$ and $\mathcal{A}_n(p)$ are the complex coefficient and the amplitude for the n^{th} intermediate process, respectively. The magnitude ρ_n and phase ϕ_n are free parameters in the fit. We use covariant tensors to construct amplitudes, which are written as

$$\mathcal{A}_n(p_j) = P_n^1 P_n^2 S_n X_n^1 X_n^2 X_n^{D^+}, \quad (4.3)$$

where S_n and $X_n^{1,2}(X_n^{D^+})$ are the spin factor and the Blatt-Weisskopf barriers for the intermediate resonances (the D^+ meson), respectively. The propagators of the two resonances, which describe the corresponding lineshapes, are indicated by $P_n^{1,2}$. Their specific forms will be introduced in Sec. 4.2.1-4.2.3.

For the amplitude of D^- decays, we define the CP conjugate phase space \bar{p}_j which is mapped to p_j by the interchange of final state charges and the reversal of three-momenta, and assume CP conservation in the D^\pm decay. Then we get

$$\mathcal{M}_{D^-}(p_j) = \sum_n c_n \bar{\mathcal{A}}_n(p_j) = \sum_n c_n \mathcal{A}_n(\bar{p}_j). \quad (4.4)$$

The background PDF is given by

$$f_B(p_j) = \frac{B(p_j) R_4(p_j)}{\int \epsilon(p_j) B(p_j) R_4(p_j) dp_j}, \quad (4.5)$$

where $B_\epsilon(p_j) = B(p_j)/\epsilon(p_j)$ is the efficiency-corrected background shape. The shape of the background in data is modeled by the background events in the signal region derived from the inclusive MC samples. The invariant mass distributions of events outside the signal region show good agreement between data and MC simulation, thus validating the description from the inclusive MC samples. We have also examined the distributions of the background events of the inclusive MC samples inside and outside the signal region. Generally, they are compatible with each other within statistical uncertainties. The background shape $B(p)$ is modeled using a kernel estimation method [25] implemented in RooFit [26] to model the distribution of an input dataset as a superposition of Gaussian kernels.

In the numerator of Eq. (4.2), the $\epsilon(p_j)$ and $R_4(p_j)$ terms are independent of the fitted variables, so they are regarded as constants in the fit. As a consequence, the log-likelihood becomes

$$\ln \mathcal{L} = \sum_k^{N_{\text{data}}} \ln \left[\omega_{\text{sig}} \frac{|\mathcal{M}(p_j)|^2}{\int \epsilon(p_j) |\mathcal{M}(p_j)|^2 R_4(p_j) dp_j} + (1 - \omega_{\text{sig}}) \frac{B_\epsilon(p_j)}{\int \epsilon(p_j) B_\epsilon(p_j) R_4(p_j) dp_j} \right]. \quad (4.6)$$

The normalization integrals of signal and background are evaluated by MC integration,

$$\begin{aligned}\int \epsilon(p_j) |\mathcal{M}(p_j)|^2 R_4(p_j) dp_j &\propto \frac{1}{N_{\text{MC}}} \sum_{k_{\text{MC}}}^{N_{\text{MC}}} \frac{|\mathcal{M}(p_j^{k_{\text{MC}}})|^2}{|\mathcal{M}^{\text{gen}}(p_j^{k_{\text{MC}}})|^2}, \\ \int \epsilon(p_j) B_\epsilon(p_j) R_4(p_j) dp_j &\propto \frac{1}{N_{\text{MC}}} \sum_{k_{\text{MC}}}^{N_{\text{MC}}} \frac{B_\epsilon(p_j^{k_{\text{MC}}})}{|\mathcal{M}^{\text{gen}}(p_j^{k_{\text{MC}}})|^2},\end{aligned}\tag{4.7}$$

where k_{MC} is the index of the k^{th} event of the MC sample and N_{MC} is the number of selected MC events. The $\mathcal{M}^{\text{gen}}(p_j)$ is the signal PDF used to generate the MC samples in MC integration.

Tracking, PID, as well as π^0 and K_S^0 reconstruction efficiency differences between data and MC simulation are corrected by multiplying the weight of the MC events by a factor γ_ϵ , which is calculated as

$$\gamma_\epsilon(p_j) = \prod_n \frac{\epsilon_{n,\text{data}}(p_j)}{\epsilon_{n,\text{MC}}(p_j)},\tag{4.8}$$

where n refers to tracking, PID, π^0 reconstruction or K_S^0 reconstruction, $\epsilon_{n,\text{data}}(p_j)$ and $\epsilon_{n,\text{MC}}(p_j)$ are their efficiencies as a function of the momenta of the daughter particles for data and MC simulation, respectively. The specific values of these efficiencies are obtained using different control samples, more detailed information will be given as part of the systematic uncertainty studies for the BF measurement. By weighting each signal MC event with γ_ϵ , the MC integration is modified to be

$$\int \epsilon(p_j) |\mathcal{M}(p_j)|^2 R_4(p_j) dp_j \propto \frac{1}{N_{\text{MC}}} \sum_{k_{\text{MC}}}^{N_{\text{MC}}} \frac{\gamma_\epsilon(p_j^{k_{\text{MC}}}) |\mathcal{M}(p_j^{k_{\text{MC}}})|^2}{|\mathcal{M}^{\text{gen}}(p_j^{k_{\text{MC}}})|^2}.\tag{4.9}$$

$$\int \epsilon(p_j) B_\epsilon(p_j) R_4(p_j) dp_j \propto \frac{1}{N_{\text{MC}}} \sum_{k_{\text{MC}}}^{N_{\text{MC}}} \frac{\gamma_\epsilon(p_j^{k_{\text{MC}}}) B_\epsilon(p_j^{k_{\text{MC}}})}{|\mathcal{M}^{\text{gen}}(p_j^{k_{\text{MC}}})|^2}.\tag{4.10}$$

4.2.1 Blatt-Weisskopf barriers

For a decay process $a \rightarrow b c$, the Blatt-Weisskopf barrier factors [27] depend on the angular momentum L and the momentum q of the final-state particle b or c in the rest system of a . They are taken as

$$\begin{aligned}X_{L=0}(q) &= 1, \\ X_{L=1}(q) &= \sqrt{\frac{z_0^2 + 1}{z^2 + 1}}, \\ X_{L=2}(q) &= \sqrt{\frac{z_0^4 + 3z_0^2 + 9}{z^4 + 3z^2 + 9}},\end{aligned}\tag{4.11}$$

where $z = qR$ and $z_0 = q_0R$. The effective radius of barrier R is fixed to be 3.0 (GeV/c)^{-1} for the intermediate resonances and 5.0 (GeV/c)^{-1} for the D^+ meson. The momentum q is given by

$$q = \sqrt{\frac{(s_a + s_b - s_c)^2}{4s_a} - s_b},\tag{4.12}$$

where s_a, s_b , and s_c are the invariant mass squared of particles a , b and c , respectively. The value of q_0 is that of q when $s_a = m_a^2$, where m_a is the mass of particle a .

4.2.2 Propagator

The intermediate resonances $a_1(1260)^+$, \bar{K}^{*0} , $K_1(1270)^+$ and $\bar{K}_1(1400)^0$ are parameterized with the relativistic Breit-Wigner (RBW) formulas,

$$\begin{aligned} P(m) &= \frac{1}{(m_0^2 - m^2) - im_0\Gamma(m)}, \\ \Gamma(m) &= \Gamma_0 \left(\frac{q}{q_0}\right)^{2L+1} \left(\frac{m_0}{m}\right) \left(\frac{X_L(q)}{X_L(q_0)}\right)^2, \end{aligned} \quad (4.13)$$

where m^2 is the invariant mass squared of the daughter particles of the intermediate resonances, and m_0 and Γ_0 are the mass and width of the intermediate resonance, which are fixed to their known values [21]. The energy-dependent width is denoted by $\Gamma(m)$.

The $a_1(1260)^+$ decays through a quasi-three-body process $r \rightarrow abc$, whose energy-dependent width is more complicated and has no analytic expression in general. Therefore, we integrate the transition amplitude squared over the three-body phase space R_3 [28]

$$\Gamma_{r \rightarrow abc}(m) = \frac{1}{2\sqrt{s}} \int |\mathcal{A}_{r \rightarrow abc}|^2 dR_3. \quad (4.14)$$

The three-body amplitude $\mathcal{A}_{r \rightarrow abc}$ can be parameterized similarly to the four-body amplitude and is obtained from the amplitude analysis of this work. Figure 3 shows the energy-dependent width for the $a_1(1260)^+$ resonance.

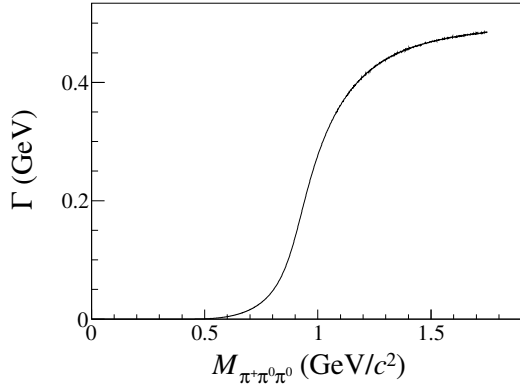


Figure 3. The energy-dependent width for the $a_1(1260)^+$.

The ρ^+ meson is parameterized using the Gounaris-Sakurai (GS) line shape [29], which is given by

$$P_{\text{GS}}(m) = \frac{1 + d\frac{\Gamma_0}{m_0}}{(m_0^2 - m^2) + f(m) - im_0\Gamma(m)}, \quad (4.15)$$

where

$$f(m) = \Gamma_0 \frac{m_0^2}{q_0^3} \left[q^2(h(m) - h(m_0)) + (m_0^2 - m^2)q_0^2 \frac{dh}{d(m^2)} \Big|_{m^2=m_0^2} \right] \quad (4.16)$$

and the function $h(m)$ is defined as

$$h(m) = \frac{2}{\pi} \frac{q}{m} \ln \left(\frac{m + 2q}{2m_\pi} \right), \quad (4.17)$$

with

$$\left. \frac{dh}{d(m^2)} \right|_{m^2=m_0^2} = h(m_0)[(8q_0^2)^{-1} - (2m_0^2)^{-1}] + (2\pi m_0^2)^{-1}, \quad (4.18)$$

where m_π is the known mass of the π [21], and the normalization condition at $P_{\text{GS}}(0)$ fixes the parameter $d = \frac{f(0)}{\Gamma_0 m_0}$. It is found to be

$$d = \frac{3}{\pi} \frac{m_\pi^2}{q_0^2} \ln \left(\frac{m_0 + 2q_0}{2m_\pi} \right) + \frac{m_0}{2\pi q_0} - \frac{m_\pi^2 m_0}{\pi q_0^3}. \quad (4.19)$$

The $f_0(980)$ is parameterized with the Flatté formula [30]:

$$P_{f_0(980)} = \frac{1}{M_{f_0(980)}^2 - m^2 - i(g_{\pi\pi}\rho_{\pi\pi}(m^2) + g_{K\bar{K}}\rho_{K\bar{K}}(m^2))}, \quad (4.20)$$

where $g_{\pi\pi, K\bar{K}}$ are the coupling constants to individual final states. The parameters are fixed to be $g_{\pi\pi} = (0.165 \pm 0.010 \pm 0.015) \text{ GeV}^2/c^4$, $g_{K\bar{K}} = (4.21 \pm 0.25 \pm 0.21)g_{\pi\pi}$ and $M = 0.965 \text{ GeV}/c^2$, as reported in Ref. [30]. The Lorentz invariant phase space factors $\rho_{\pi\pi}(s)$ and $\rho_{K\bar{K}}(s)$ are given by

$$\begin{aligned} \rho_{\pi\pi} &= \frac{2}{3} \sqrt{1 - \frac{4m_{\pi^\pm}^2}{m^2}} + \frac{1}{3} \sqrt{1 - \frac{4m_{\pi^0}^2}{m^2}}, \\ \rho_{K\bar{K}} &= \frac{1}{2} \sqrt{1 - \frac{4m_{K^\pm}^2}{m^2}} + \frac{1}{2} \sqrt{1 - \frac{4m_{K^0}^2}{m^2}}. \end{aligned} \quad (4.21)$$

The resonance $f_0(500)$ is parameterized with the formula given in Ref. [31]:

$$P_{f_0(500)} = \frac{1}{m_0^2 - m^2 - im_0\Gamma_{\text{tot}}(m)}, \quad (4.22)$$

where $\Gamma_{\text{tot}}(m)$ is decomposed into two parts:

$$\Gamma_{\text{tot}}(m) = g_{\pi\pi} \frac{\rho_{\pi\pi}(m)}{\rho_{\pi\pi}(m_0)} + g_{4\pi} \frac{\rho_{4\pi}(m)}{\rho_{4\pi}(m_0)} \quad (4.23)$$

and

$$g_{\pi\pi} = (b_1 + b_2 m^2) \left(\frac{m^2 - m_\pi^2/2}{m_0^2 - m_\pi^2/2} \right) e^{(m_0^2 - m^2)/a}, \quad (4.24)$$

where $\rho_{\pi\pi}$ and $\rho_{4\pi}$ are the phase space of the $\pi^+\pi^-$ and 4π systems, respectively. They are approximated by

$$\rho_{\pi\pi} = \sqrt{\left(1 - \frac{4m_\pi^2}{m^2}\right)}, \quad \rho_{4\pi} = \sqrt{\left(1 - \frac{16m_\pi^2}{m^2}\right)} / (1 + e^{3.5(2.8 - m^2)}), \quad (4.25)$$

with the parameters fixed to the values given in Ref. [32].

The $K\pi$ S-wave modeled by the LASS parameterization [33] is described by a $K_0^*(1430)$ Breit-Wigner together with an effective range non-resonant component with a phase shift. It is given by

$$A(m) = F \sin \delta_F e^{i\delta_F} + R \sin \delta_R e^{i\delta_R} e^{i2\delta_F}, \quad (4.26)$$

with

$$\begin{aligned} \delta_F &= \phi_F + \cot^{-1} \left[\frac{1}{aq} + \frac{rq}{2} \right], \\ \delta_R &= \phi_R + \tan^{-1} \left[\frac{M\Gamma(m_{K\pi})}{M^2 - m_{K\pi}^2} \right], \end{aligned} \quad (4.27)$$

where the parameters $F(\phi_F)$ and $R(\phi_R)$ are the magnitudes (phases) for non-resonant state and resonance terms, respectively. The parameters a and r are the scattering length and effective interaction length, respectively. We fix these parameters ($M, \Gamma, F, \phi_F, R, \phi_R, a, r$) to the results obtained from the amplitude analysis to a sample of $D^0 \rightarrow K_S^0 \pi^+ \pi^-$ by the *BABAR* and Belle experiments [34]; these parameters are summarised in table 1.

M (GeV/ c^2)	1.441 ± 0.002
Γ (GeV)	0.193 ± 0.004
F	0.96 ± 0.07
ϕ_F ($^\circ$)	0.1 ± 0.3
R	1(fixed)
ϕ_R ($^\circ$)	-109.7 ± 2.6
a (GeV/ c) $^{-1}$	0.113 ± 0.006
r (GeV/ c) $^{-1}$	-33.8 ± 1.8

Table 1. The $K\pi$ S-wave parameters, obtained from the amplitude analysis of $D^0 \rightarrow K_S^0 \pi^+ \pi^-$ by the *BABAR* and Belle experiments [34]. Uncertainties are statistical only.

4.2.3 Spin factors

Due to the limited size of phase space, we only consider states with angular momenta below three. For a two-body decay, $a \rightarrow bc$, we use the notation p_a , p_b and p_c as the momenta of particles a , b and c , respectively, and let $r_a = p_b - p_c$ be the break-up four-momentum. The spin projection operators are defined as

$$\begin{aligned} P^0(a) &= 1, & (S \text{ wave}) \\ P_{\mu\nu}^{(1)}(a) &= -g_{\mu\nu} + \frac{p_{a\mu} p_{a\nu}}{p_a^2}, & (P \text{ wave}) \\ P_{\mu_1\mu_2\nu_1\nu_2}^{(2)}(a) &= \frac{1}{2}(P_{\mu_1\nu_1}^{(1)} P_{\mu_2\nu_2}^{(1)} + P_{\mu_1\nu_2}^{(1)} P_{\mu_2\nu_1}^{(1)}) - \frac{1}{3}P_{\mu_1\mu_2}^{(1)} P_{\nu_1\nu_2}^{(1)}. & (D \text{ wave}) \end{aligned} \quad (4.28)$$

The covariant tensors are given by

$$\begin{aligned} \tilde{t}^{(0)}(a) &= 1, & (S \text{ wave}) \\ \tilde{t}_\mu^{(1)}(a) &= -P_{\mu\nu}^{(1)}(a) r_a^\nu, & (P \text{ wave}) \\ \tilde{t}_{\mu\nu}^{(2)}(a) &= P_{\mu\mu_1\nu\nu_1}^{(2)}(a) r_a^{\mu_1} r_a^{\nu_1}. & (D \text{ wave}) \end{aligned} \quad (4.29)$$

The spin factors $S(p)$ used in this work are constructed from the spin projection operators and pure orbital angular-momentum covariant tensors and are listed in table 2.

Decay chain	$S(p)$
$D^+[S] \rightarrow V_1 V_2$	$\tilde{t}^{(1)\mu}(V_1)\tilde{t}_\mu^{(1)}(V_2)$
$D^+[P] \rightarrow V_1 V_2$	$\epsilon_{\mu\nu\lambda\sigma}p^\mu(D^+)\tilde{T}^{(1)\nu}(D^+)\tilde{t}^{(1)\lambda}(V_1)\tilde{t}^{(1)\sigma}(V_2)$
$D^+[D] \rightarrow V_1 V_2$	$\tilde{T}^{(2)\mu\nu}(D^+)\tilde{t}_\mu^{(1)}(V_1)\tilde{t}_\nu^{(1)}(V_2)$
$D^+ \rightarrow AP_1, A[S] \rightarrow VP_2$	$\tilde{T}^{(1)\mu}(D^+)P_{\mu\nu}^{(1)}(A)\tilde{t}^{(1)\nu}(V)$
$D^+ \rightarrow AP_1, A[D] \rightarrow VP_2$	$\tilde{T}^{(1)\mu}(D^+)\tilde{t}_{\mu\nu}^{(2)}(A)\tilde{t}^{(1)\nu}(V)$
$D^+ \rightarrow AP_1, A \rightarrow SP_2$	$\tilde{T}^{(1)\mu}(D^+)\tilde{t}_\mu^{(1)}(A)$
$D^+ \rightarrow VS$	$\tilde{T}^{(1)\mu}(D^+)\tilde{t}_\mu^{(1)}(V)$
$D^+ \rightarrow V_1 P_1, V_1 \rightarrow V_2 P_2$	$\epsilon_{\mu\nu\lambda\sigma}p_{V_1}^\mu r_{V_1}^\nu p_{P_1}^\lambda r_{V_2}^\sigma$
$D^+ \rightarrow PP_1, P \rightarrow VP_2$	$p^\mu(P_2)\tilde{t}_\mu^{(1)}(V)$
$D^+ \rightarrow TS$	$\tilde{T}^{(2)\mu\nu}(D^+)\tilde{t}_{\mu\nu}^{(2)}(T)$

Table 2. The spin factor $S(p)$ for each decay chain. All operators, i.e. \tilde{t} and \tilde{T} , have the same definitions as in Ref. [35]. Scalar, pseudo-scalar, vector, axial-vector and tensor states are denoted by S , P , V , A and T , respectively. The $[S]$, $[P]$ and $[D]$ denote the orbital angular-momentum quantum numbers $L = 0, 1$ and 2 , respectively.

4.3 Fit results

With the method described in Sec. 4.2, we perform the fit in steps, by adding intermediate processes one by one. Based on previous analyses [36, 37], the process $D^+ \rightarrow K_S^0 a_1(1260)^+[S](\rightarrow \rho^+\pi^0)$ is expected to have the largest fitting fraction (FF). Hence its magnitude and phase are fixed to 1.0 and 0.0 as reference, respectively, while those of other processes are floating. The ω_{sig} value in Eq. (4.6) is fixed to the purity given in Sec. 4.1.

Since \bar{K}^{*0} and ρ^+ peaks are clearly observed in the corresponding invariant mass spectra, we try to add $D^+ \rightarrow \bar{K}^{*0}\rho^+$ first, as well as a few processes including these two mesons. Then we test other possible intermediate resonances, including $\bar{K}_1(1400)^0$, $K_1(1270)^+$, $f_0(500)$, $f_0(980)$, $(K^+\pi^-)_{S\text{-wave}}$, etc. Finally, amplitudes for $D^+ \rightarrow K_S^0 a_1(1260)^+[S](\rightarrow \rho^+\pi^0)$, $D^+ \rightarrow K_S^0 a_1(1260)^+(\rightarrow f_0(500)\pi^+)$, $D^+ \rightarrow \bar{K}_1(1400)^0(\rightarrow \bar{K}^{*0}\pi^0)\pi^+$, $D^+ \rightarrow \bar{K}^{*0}\rho^+$, $D^+ \rightarrow \bar{K}^{*0}(\pi^+\pi^0)_V$, and $D^+ \rightarrow K_S^0(\rho^+\pi^0)_P$, which have statistical significance greater than 5 standard deviations, are retained in the nominal fit. The statistical significance of each process is determined from the changes in log-likelihood and the numbers of degrees of freedom when the fits are performed with and without the process included.

Generator-level MC events without detector acceptance and resolution effects are used to calculate the FFs for individual amplitudes. The FF for the n^{th} amplitude is defined as

$$\text{FF}_n = \frac{\sum_{N_{\text{gen}}} |c_n \mathcal{A}_n|^2}{\sum_{N_{\text{gen}}} |\mathcal{M}|^2}, \quad (4.30)$$

where N_{gen} is the number of phase space MC events at the generator level. The sum of these FFs is generally not unity due to net constructive or destructive interference.

Interference (IN) between the n^{th} and n'^{th} amplitudes is defined as

$$\text{IN}_{nn'} = \frac{\sum^{N_{\text{gen}}} 2\text{Re}[c_n c_{n'}^* \mathcal{A}_n \mathcal{A}_{n'}^*]}{\sum^{N_{\text{gen}}} |\mathcal{M}|^2}. \quad (4.31)$$

The statistical uncertainties of the FFs are obtained by randomly perturbing the fit parameters according to their uncertainties and the covariance matrix and re-evaluating FFs. A Gaussian function is used to fit the resulting distribution for each FF and the fitted width is taken as its statistical uncertainty.

According to the fit result, the phases, FFs and statistical significances for various amplitudes are listed in table 3. The interference between processes is listed in table 8 of appendix C. The statistical significances for the processes tested but not included in the nominal fit are listed in appendix B. The mass projections of the nominal fit are shown in figure 4.

Amplitude	Phase ϕ_n (rad)	FF (%)	Significance (σ)
$D^+ \rightarrow K_S^0 a_1(1260)^+ [S](\rightarrow \rho^+ \pi^0)$	0.0 (fixed)	$30.0 \pm 3.6 \pm 4.2$	>10
$D^+ \rightarrow K_S^0 a_1(1260)^+ (\rightarrow f_0(500) \pi^+)$	$4.78 \pm 0.22 \pm 0.20$	$3.5 \pm 1.1 \pm 1.9$	6.9
$D^+ \rightarrow \bar{K}_1(1400)^0 [S](\rightarrow \bar{K}^{*0} \pi^0) \pi^+$	$-3.01 \pm 0.12 \pm 0.16$	$6.0 \pm 1.2 \pm 0.3$	9.6
$D^+ \rightarrow \bar{K}_1(1400)^0 [D](\rightarrow \bar{K}^{*0} \pi^0) \pi^+$	$4.29 \pm 0.16 \pm 0.20$	$2.4 \pm 0.6 \pm 0.2$	6.7
$D^+ \rightarrow \bar{K}_1(1400)^0 (\rightarrow \bar{K}^{*0} \pi^0) \pi^+$	-	$8.0 \pm 1.2 \pm 0.4$	-
$D^+ [S] \rightarrow \bar{K}^{*0} \rho^+$	$-3.33 \pm 0.10 \pm 0.17$	$31.8 \pm 2.7 \pm 1.3$	>10
$D^+ [P] \rightarrow \bar{K}^{*0} \rho^+$	$-1.68 \pm 0.17 \pm 0.16$	$1.7 \pm 0.6 \pm 0.1$	5.0
$D^+ \rightarrow \bar{K}^{*0} \rho^+$	-	$33.6 \pm 2.7 \pm 1.4$	-
$D^+ [S] \rightarrow \bar{K}^{*0} (\pi^+ \pi^0)_V$	$-5.60 \pm 0.13 \pm 0.16$	$9.1 \pm 2.0 \pm 1.0$	9.4
$D^+ \rightarrow K_S^0 (\rho^+ \pi^0)_P$	$0.76 \pm 0.11 \pm 0.24$	$16.5 \pm 1.6 \pm 0.3$	>10

Table 3. The phases, FFs and statistical significances for various amplitudes in the nominal fit. Groups of related amplitudes are separated by horizontal lines. The last row of each group gives the total fitting fractions of the above components with interference considered. The first and second uncertainties of the phases and FFs are statistical and systematic, respectively. The \bar{K}^{*0} resonance decays to $K_S^0 \pi^0$. The ρ^+ resonance decays to $\pi^+ \pi^0$. The $f_0(500)$ resonance decays to $\pi^0 \pi^0$. The total FF is 100.39%.

4.4 Systematic uncertainties for the amplitude analysis

The systematic uncertainties for the amplitude analysis are summarized in table 4, and are described below. The square roots of the quadratic sums of each uncertainty are considered as the total uncertainties.

- i Fixed parameters in the amplitudes. The masses and widths of \bar{K}^{*0} , ρ^+ , $a_1(1260)^+$ and $\bar{K}_1(1400)^0$ are varied by their uncertainties [21]. The uncertainties of the line-shape for the $f_0(500)$ are estimated by replacing the propagator with the RBW formula, in which the mass and width for the $f_0(500)$ are fixed at 526 MeV/ c^2 and 534 MeV, respectively [32]. Since varying the propagator results in different normalization factors, only the effect on all FFs is considered. The changes of the phases ϕ and FFs are assigned as the associated systematic uncertainties.

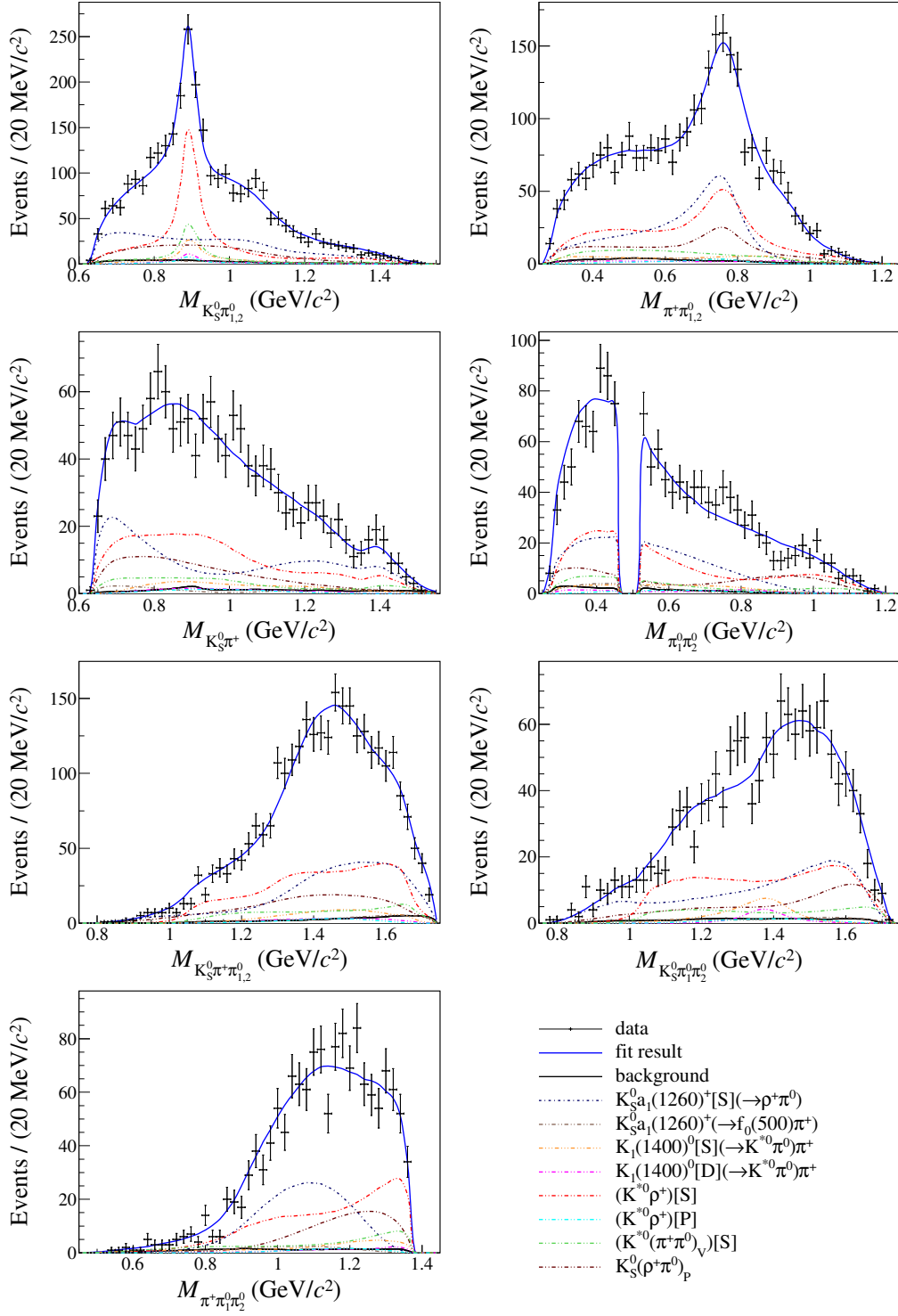


Figure 4. Projections of the nominal fit onto invariant mass distributions. The data sample is represented by points with error bars, the fit results by the solid blue lines, and the background by the solid black lines. Colored curves show the components of the fit model. The two π^0 are sorted according to the magnitude of their momentum. The labels $\pi_{1,2}^0$ mean that two distributions involving a single π^0 have been combined.

- ii R values. The estimation of the systematic uncertainty associated with the R parameters in the Blatt-Weisskopf factors is performed by repeating the fit procedure after varying the effective radius of the intermediate states and D^+ meson by $\pm 1 \text{ GeV}^{-1}$.
- iii Fit bias. An ensemble of 600 signal MC samples is generated according to the result of the amplitude analysis. The pull distributions, supposed to be normal distributions, are used to validate the fit performance and are fitted with a Gaussian function. The fitted mean values for FFs of $D^+ \rightarrow \bar{K}_1(1400)^0[S](\rightarrow \bar{K}^{*0}\pi^0)\pi^+$ deviate upward from zero by more than three standard deviations. No significant deviations are observed for other terms. We correct all FFs and phases by the fitted mean values, and assign the uncertainties of the fitted mean values as the systematic uncertainties.
- iv Background estimation. The uncertainty from the size of the background is studied by varying the signal fraction (equivalent to the fraction of background), i.e. ω_{sig} in Eq. (4.1), within its corresponding statistical uncertainty. Another source of uncertainty is the simulation of the background shape. We extract the shape with other input variables and change the fraction of different background components in MC simulation.
- v Experimental effects. The systematic uncertainty from the γ_ϵ factor in Eq. (4.9), which corrects for data-MC differences in tracking, PID as well as π^0 and K_S^0 reconstruction efficiencies, is evaluated by performing the fit after varying the weights according to their uncertainties.

5 BF measurement

The BF measurement is based on the following equations:

$$N_{\text{tag}}^{\text{ST}} = 2N_{D^+D^-} \mathcal{B}_{\text{tag}} \epsilon_{\text{tag}}^{\text{ST}}, \quad (5.1)$$

$$N_{\text{tag,sig}}^{\text{DT}} = 2N_{D^+D^-} \mathcal{B}_{\text{tag}} \mathcal{B}_{\text{sig}} \epsilon_{\text{tag,sig}}^{\text{DT}}, \quad (5.2)$$

where $N_{D^+D^-}$ is the total number of D^+D^- pairs produced in the initial e^+e^- collisions; $N_{\text{tag}}^{\text{ST}}$ is the ST yield for a specific tag mode; $N_{\text{tag,sig}}^{\text{DT}}$ is the DT yield; \mathcal{B}_{tag} and \mathcal{B}_{sig} are the BFs of the tag and the signal modes, respectively; $\epsilon_{\text{tag}}^{\text{ST}}$ is the ST efficiency to reconstruct the tag mode; $\epsilon_{\text{tag,sig}}^{\text{DT}}$ is the DT efficiency to reconstruct both the tag and the signal decay modes. The total DT yield is calculated as

$$N_{\text{total}}^{\text{DT}} = \sum_{\alpha} N_{\alpha,\text{sig}}^{\text{DT}} = \mathcal{B}_{\text{sig}} \sum_{\alpha} 2N_{D^+D^-} \mathcal{B}_{\alpha} \epsilon_{\alpha,\text{sig}}^{\text{DT}}, \quad (5.3)$$

where α represents different tag modes. By isolating \mathcal{B}_{sig} , we obtain:

$$\mathcal{B}_{\text{sig}} = \frac{N_{\text{total}}^{\text{DT}}}{\mathcal{B}_{\text{sub}} \sum_{\alpha} N_{\alpha}^{\text{ST}} \epsilon_{\alpha,\text{sig}}^{\text{DT}} / \epsilon_{\alpha}^{\text{ST}}}, \quad (5.4)$$

Amplitude		Source					Total
		i	ii	iii	iv	v	
$D^+ \rightarrow K_S^0 a_1(1260)^+ [S](\rightarrow \rho^+ \pi^0)$	FF	1.19	0.40	0.04	0.34	0.04	1.30
$D^+ \rightarrow K_S^0 a_1(1260)^+ (\rightarrow f_0(500) \pi^+)$	ϕ	0.91	0.56	0.04	0.10	0.05	1.08
	FF	1.69	0.08	0.04	0.56	0.02	1.78
$D^+ \rightarrow \bar{K}_1(1400)^0 [S](\rightarrow \bar{K}^{*0} \pi^0) \pi^+$	ϕ	1.32	0.16	0.04	0.01	0.05	1.33
	FF	0.24	0.07	0.04	0.23	0.01	0.34
$D^+ \rightarrow \bar{K}_1(1400)^0 [D](\rightarrow \bar{K}^{*0} \pi^0) \pi^+$	ϕ	1.24	0.14	0.04	0.23	0.02	1.27
	FF	0.39	0.04	0.04	0.18	0.01	0.43
$D^+ \rightarrow \bar{K}_1(1400)^0 (\rightarrow \bar{K}^{*0} \pi^0) \pi^+$	FF	0.33	0.10	0.04	0.29	0.01	0.45
$D^+ [S] \rightarrow \bar{K}^{*0} \rho^+$	ϕ	1.67	0.17	0.04	0.02	0.06	1.68
	FF	0.50	0.32	0.04	0.03	0.02	0.60
$D^+ [P] \rightarrow \bar{K}^{*0} \rho^+$	ϕ	0.94	0.09	0.04	0.07	0.01	0.95
	FF	0.16	0.04	0.04	0.14	0.00	0.22
$D^+ \rightarrow \bar{K}^{*0} \rho^+$	FF	0.52	0.32	0.04	0.00	0.02	0.61
$D^+ [S] \rightarrow \bar{K}^{*0} (\pi^+ \pi^0)_V$	ϕ	1.20	0.06	0.04	0.03	0.05	1.20
	FF	0.51	0.22	0.04	0.11	0.02	0.57
$D^+ \rightarrow K_S^0 (\rho^+ \pi^0)_P$	ϕ	2.20	0.58	0.05	0.38	0.10	2.31
	FF	0.17	0.32	0.04	0.02	0.02	0.37

Table 4. Systematic uncertainties on the ϕ and FF for each amplitude in units of the corresponding statistical uncertainty. The sources are: (i) fixed parameters in the amplitudes, (ii) R values, (iii) fit bias, (iv) background estimation, (v) experimental effects.

where $\mathcal{B}_{\text{sub}} = \mathcal{B}_{K_S^0 \rightarrow \pi^+ \pi^-} \mathcal{B}_{\pi^0 \rightarrow \gamma \gamma}^2$ is introduced to take into account the fact that the signal is reconstructed through these decays. The yields $N_{\text{total}}^{\text{DT}}$ and N_{α}^{ST} are obtained from the data sample, while $\epsilon_{\alpha}^{\text{ST}}$ and $\epsilon_{\alpha, \text{sig}}^{\text{DT}}$ can be obtained from the inclusive and signal MC samples in which $D^+ \rightarrow K_S^0 \pi^+ \pi^0 \pi^0$ events are generated according to the result of the amplitude analysis, respectively.

Six tag modes used in the BF measurement and their energy difference requirements are listed in table 5. For multiple ST candidates, the one with minimum $|\Delta E|$ is chosen. The ST yields ($N_{\text{tag}}^{\text{ST}}$) and efficiencies ($\epsilon_{\text{tag}}^{\text{ST}}$) for each tag mode, also listed in table 5, are obtained by fitting the corresponding $M_{\text{BC}}^{\text{tag}}$ distributions individually. In the fit, the signal is modeled by a MC-simulated shape convolved with a Gaussian function which describes the resolution difference between data and MC simulation. The background is described by the ARGUS [38] function whose parameters are left floating except for the endpoint, which is fixed at 1.8865 GeV. Figure 5 shows the fit results.

Once a tag mode is identified, we search for the signal decay $D^+ \rightarrow K_S^0 \pi^+ \pi^0 \pi^0$ on the recoiling side using the condition $\Delta E_{\text{sig}} \in [-0.063, 0.034]$ GeV. An unbinned 2D maximum likelihood fit is used to get the DT yield. In addition to the signal and background PDFs in appendix A, one additional PDF based on a MC simulated shape is employed

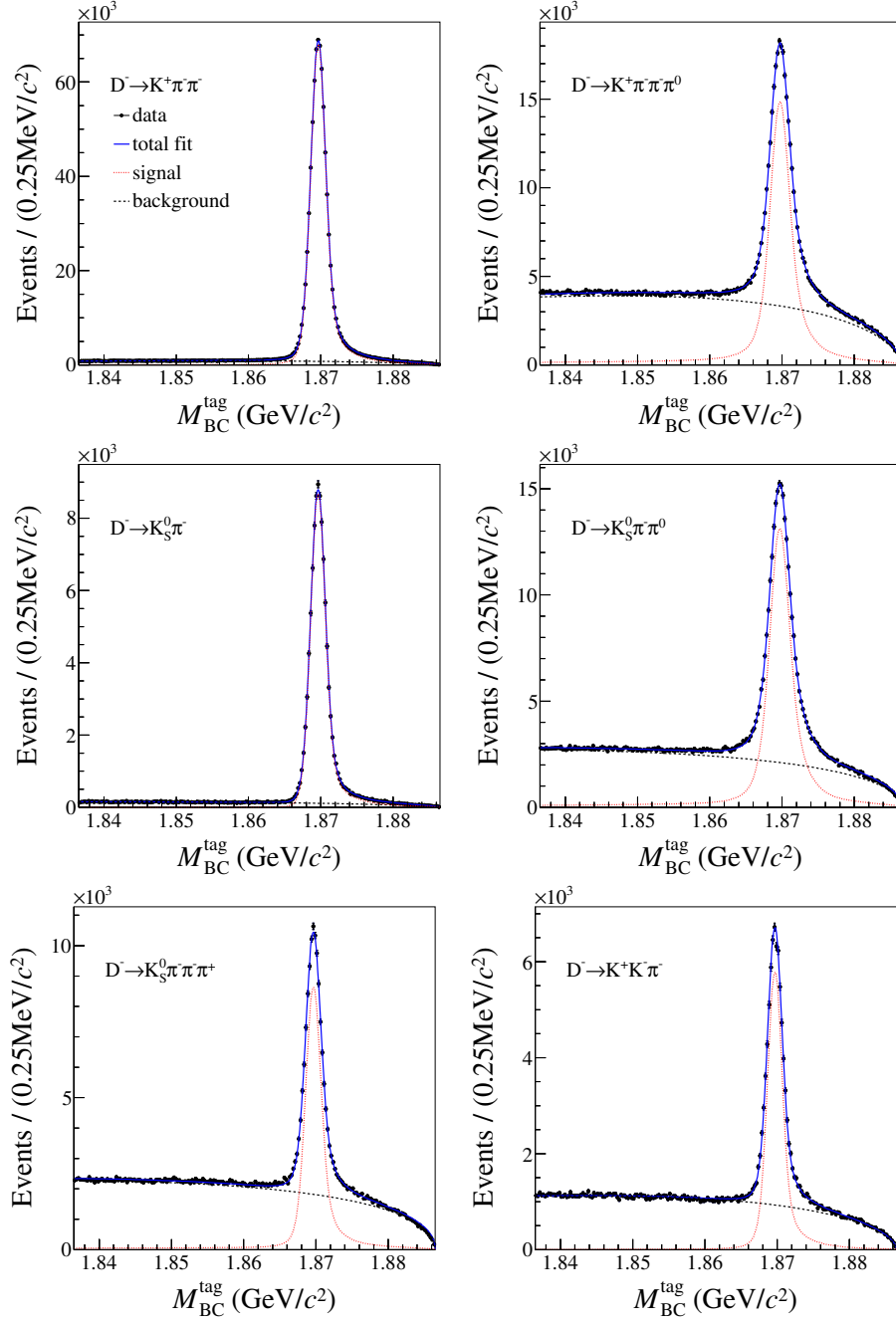


Figure 5. Fits to the M_{BC}^{tag} distribution of the ST candidates. The dots with error bars are data, the solid blue lines are the total fit, the black dashed lines represent the background shape, the red dashed lines represent the signal shape.

Tag mode	ΔE (MeV)	$N_{\text{tag}}^{\text{ST}}$	$\epsilon_{\text{tag}}^{\text{ST}}$ (%)	$\epsilon_{\text{tag,sig}}^{\text{DT}}$ (%)	ϵ_{sig} (%)
$D^- \rightarrow K^+ \pi^- \pi^-$	(-25, 25)	821313 ± 974	52.65 ± 0.02	6.46 ± 0.01	12.27 ± 0.02
$D^- \rightarrow K^+ \pi^- \pi^- \pi^0$	(-55, 40)	285779 ± 855	29.37 ± 0.03	2.99 ± 0.01	10.19 ± 0.03
$D^- \rightarrow K_S^0 \pi^-$	(-25, 25)	101444 ± 339	55.38 ± 0.07	6.71 ± 0.03	12.12 ± 0.05
$D^- \rightarrow K_S^0 \pi^- \pi^0$	(-55, 40)	249765 ± 766	30.72 ± 0.03	3.25 ± 0.01	10.58 ± 0.03
$D^- \rightarrow K_S^0 \pi^- \pi^- \pi^+$	(-25, 25)	119226 ± 493	30.02 ± 0.04	3.46 ± 0.01	11.53 ± 0.04
$D^- \rightarrow K^+ K^- \pi^-$	(-25, 25)	70825 ± 337	42.75 ± 0.07	5.18 ± 0.02	12.11 ± 0.06

Table 5. The ΔE requirements, ST yields ($N_{\text{tag}}^{\text{ST}}$), ST efficiencies ($\epsilon_{\text{tag}}^{\text{ST}}$), DT efficiencies ($\epsilon_{\text{tag,sig}}^{\text{DT}}$) and signal efficiencies ($\epsilon_{\text{sig}} = \epsilon_{\text{tag,sig}}^{\text{DT}}/\epsilon_{\text{tag}}^{\text{ST}}$) for six tag modes. The uncertainties are statistical only.

to describe the peaking background from $D^+ \rightarrow K_S^0 K_S^0 \pi^+$. The corresponding yield is fixed to the estimation from the MC simulation. In order to estimate the combinatorial $\pi^+ \pi^-$ backgrounds from K_S^0 reconstruction, we define the K_S^0 sideband region by $20 < |M_{\pi^+ \pi^-} - M_{K_S^0}| < 44$ MeV/ c^2 and perform the 2D fit in the K_S^0 signal and the sideband region, respectively. By subtracting the sideband contribution, the DT yield is calculated by

$$N_{\text{total}}^{\text{DT}} = N_{K_S^0, \text{sig}}^{\text{DT}} - \frac{1}{2} N_{K_S^0, \text{side}}^{\text{DT}}, \quad (5.5)$$

where $N_{K_S^0, \text{sig}}^{\text{DT}}$ and $N_{K_S^0, \text{side}}^{\text{DT}}$ denote the fitted yields in the K_S^0 signal and sideband regions, which are 3812 ± 74 and 266 ± 23 , respectively. This relation has been verified by a large MC sample. Finally, the DT yield is obtained to be 3679 ± 75 and the fit results are shown in figure 6. Using a similar method for the signal MC samples, the DT efficiencies for various tag modes are determined and listed in table 5.

After correcting for the differences in π^\pm tracking, PID and π^0 reconstruction efficiencies between data and MC simulation, we determine the BF to be $\mathcal{B}(D^+ \rightarrow K_S^0 \pi^+ \pi^0 \pi^0) = (2.888 \pm 0.058_{\text{stat.}} \pm 0.069_{\text{syst.}})\%$.

Most systematic uncertainties related to the efficiency of reconstructing the D^\pm mesons on the tag side cancel due to the DT method. The following sources are taken into consideration to evaluate the systematic uncertainties in the BF measurement.

- ST yield. The uncertainty of the total yield of the ST D^\pm mesons has previously been estimated to be 0.5% [39–41], and is mainly due to the fits to the M_{BC} distributions of ST candidates.
- Tracking and PID efficiencies. The data-MC efficiency ratios for π^+ tracking and PID efficiencies are determined to be 1.001 ± 0.001 and 0.998 ± 0.001 for this decay channel by studying DT $D\bar{D}$ hadronic events. After correcting the MC efficiencies to data by these factors, the statistical uncertainties of the correction parameters are assigned to be the systematic uncertainties, which are 0.1% for both π^+ tracking and PID.
- K_S^0 reconstruction. This systematic uncertainty is estimated from the measurements of $J/\psi \rightarrow K^*(892)^\mp K^\pm$ and $J/\psi \rightarrow \phi K_S^0 K^\pm \pi^\mp$ control samples [42] and found to be 1.6% per K_S^0 .

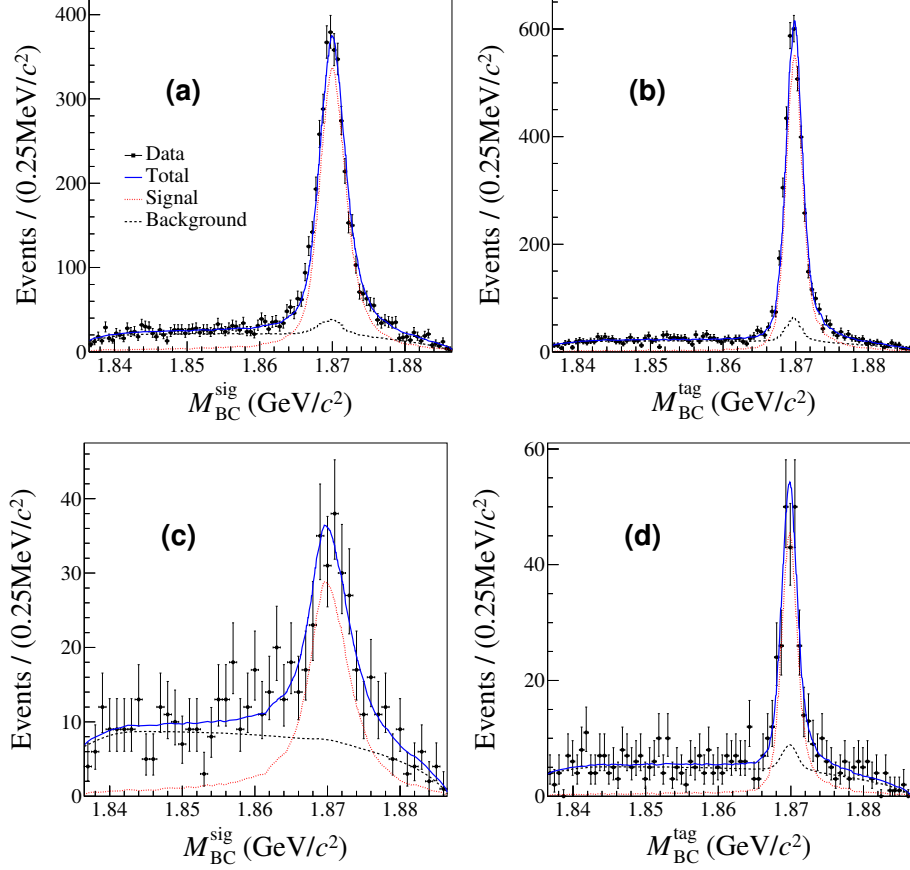


Figure 6. The projections of the 2D fit of $M_{\text{BC}}^{\text{sig}}$ versus $M_{\text{BC}}^{\text{tag}}$ for data in the K_S^0 signal region (a)(b) and sideband region (c)(d). The black points with error bars are data. The blue solid lines are the total fits. The red dotted and black dashed lines are the fitted signal and background, respectively.

- π^0 reconstruction. The data-MC efficiency ratio for π^0 reconstruction is determined to be 0.994 ± 0.007 by using the $D\bar{D}$ hadronic decay samples of $D^0 \rightarrow K^-\pi^+$, $K^-\pi^+\pi^+\pi^-$ versus $\bar{D}^0 \rightarrow K^+\pi^-\pi^0$, $K_S^0\pi^0$. After correcting the efficiency by this factor for each π^0 , we assign 0.7% as the systematic uncertainty arising from the reconstruction of each π^0 .
- MC sample size. The uncertainty of the limited MC sample size is given by $\sqrt{\sum_{\alpha} (\frac{f_{\alpha}\delta\epsilon_{\alpha}}{\epsilon_{\alpha}})^2}$, where f_{α} is the tag yield fraction, ϵ_{α} is the average DT efficiency of tag mode α and $\delta\epsilon_{\alpha}$ is the uncertainty of ϵ_{α} . The corresponding uncertainty is determined to be 0.6%.
- Quoted BFs. In this measurement, the BFs of the daughter particles are quoted from the PDG [21], which are $\mathcal{B}(\pi^0 \rightarrow \gamma\gamma) = (98.82 \pm 0.04)\%$ and $\mathcal{B}(K_S^0 \rightarrow \pi^+\pi^-) = (69.20 \pm 0.05)\%$. The associated uncertainty is assigned to be 0.1%.
- Amplitude model. The uncertainty from the amplitude model is determined by varying the amplitude model parameters based on their error matrix 600 times. A Gaus-

sian function is used to fit the distribution of 600 DT efficiencies and the fitted width divided by the mean value is taken as the systematic uncertainty, which is 0.6%.

- 2D fit. The signal and background shapes as well as the estimation of the size of the peaking background are the possible sources of uncertainty from the 2D fit. We vary the mean and width of the smeared Gaussian by $\pm 1\sigma$ for the signal shape and the ARGUS end-point by $\pm 0.2 \text{ MeV}/c^2$ for the background shape. Considering the uneven distribution for combinatorial $\pi^+\pi^-$ backgrounds of K_S^0 reconstruction, we also vary the $\frac{1}{2}$ factor in Eq. (5.5) according to its uncertainty from MC simulation. For the peaking background $D^+ \rightarrow K_S^0 K_S^0 \pi^+$, whose yield is fixed in the 2D fit, we vary the quoted BF of this decay by $\pm 1\sigma$. The quadratic sum of the relative BF changes, 0.5%, is assigned to be the systematic uncertainty for the 2D fit.
- ΔE_{sig} requirement. Considering the possible difference between data and MC simulation, we examine the ΔE_{sig} cut efficiency after smearing a double-Gaussian function for signal MC sample and we take the change of this efficiency to be the systematic uncertainty, which is 0.4%.

All the systematic uncertainties are summarized in table 6. Adding them in quadrature results in a total systematic uncertainty of 2.6% in the BF measurement.

Source	Uncertainty (%)
ST yield	0.5
Tracking efficiency	0.1
PID efficiency	0.1
K_S^0 reconstruction	1.6
π^0 reconstruction	1.4
MC sample size	0.6
Quoted BFs	0.1
Amplitude model	0.6
2D fit	0.5
ΔE_{sig} requirement	0.4
Total	2.4

Table 6. Systematic uncertainties in the BF measurement.

6 Summary

Using an e^+e^- collision data sample with an integrated luminosity of 2.93 fb^{-1} collected by the BESIII detector at $\sqrt{s} = 3.773 \text{ GeV}$, an amplitude analysis of $D^+ \rightarrow K_S^0 \pi^+ \pi^0 \pi^0$ is performed for the first time. The results for phases and FFs of different intermediate processes are listed in table 3. With the detection efficiency obtained from a signal MC sample, which is generated based on our amplitude analysis model, the BF is determined to be $\mathcal{B}(D^+ \rightarrow K_S^0 \pi^+ \pi^0 \pi^0) = (2.888 \pm 0.058_{\text{stat.}} \pm 0.069_{\text{syst.}})\%$. It is consistent with the

previous BESIII result $(2.904 \pm 0.062_{\text{stat.}} \pm 0.087_{\text{syst.}})\%$ [3] within 1σ , where the detection efficiency was simulated using mixed-signal MC samples.

Intermediate process	BF ($\times 10^{-3}$)
$D^+ \rightarrow K_S^0 a_1(1260)^+[S](\rightarrow \rho^+\pi^0)$	$8.66 \pm 1.04 \pm 1.24$
$D^+ \rightarrow K_S^0 a_1(1260)^+(\rightarrow f_0(500)\pi^+)\pi^+$	$1.00 \pm 0.33 \pm 0.55$
$D^+ \rightarrow \bar{K}_1(1400)^0[S](\rightarrow \bar{K}^{*0}\pi^0)\pi^+$	$1.73 \pm 0.34 \pm 0.09$
$D^+ \rightarrow \bar{K}_1(1400)^0[D](\rightarrow \bar{K}^{*0}\pi^0)\pi^+$	$0.68 \pm 0.16 \pm 0.07$
$D^+ \rightarrow \bar{K}_1(1400)^0(\rightarrow \bar{K}^{*0}\pi^0)\pi^+$	$2.32 \pm 0.36 \pm 0.13$
$D^+[S] \rightarrow \bar{K}^{*0}\rho^+$	$9.20 \pm 0.80 \pm 0.45$
$D^+[P] \rightarrow \bar{K}^{*0}\rho^+$	$0.49 \pm 0.17 \pm 0.03$
$D^+ \rightarrow \bar{K}^{*0}\rho^+$	$9.70 \pm 0.81 \pm 0.47$
$D^+[S] \rightarrow \bar{K}^{*0}(\pi^+\pi^0)_V$	$2.63 \pm 0.57 \pm 0.30$
$D^+ \rightarrow K_S^0(\rho^+\pi^0)_P$	$4.75 \pm 0.46 \pm 0.14$

Table 7. The BFs for intermediate processes with the final state $D^+ \rightarrow K_S^0\pi^+\pi^0\pi^0$. The uncertainties are statistical and systematical respectively. Here, \bar{K}^{*0} decays to $K_S^0\pi^0$, ρ^+ decays to $\pi^+\pi^0$, and $f_0(500)$ decays to $\pi^0\pi^0$.

We find $D^+ \rightarrow \bar{K}^{*0}\rho^+$ and $D^+ \rightarrow K_S^0 a_1(1260)^+[S](\rightarrow \rho^+\pi^0)$ dominate in $D^+ \rightarrow K_S^0\pi^+\pi^0\pi^0$ with FFs of $(33.6 \pm 2.7_{\text{stat.}} \pm 1.4_{\text{syst.}})\%$ and $(30.0 \pm 3.6_{\text{stat.}} \pm 4.2_{\text{syst.}})\%$, respectively, and obtain the BFs for intermediate processes presented in table 7.

The absolute BF for $D^+ \rightarrow \bar{K}^{*0}\rho^+$ is determined to be $(5.82 \pm 0.49_{\text{stat.}} \pm 0.28_{\text{syst.}})\%$, which is consistent with the MARK III result $(4.8 \pm 1.2_{\text{stat.}} \pm 1.4_{\text{syst.}})\%$ [7] within 1σ but much more precise. The measured BF of $D^+ \rightarrow K_S^0 a_1(1260)^+[S](\rightarrow \rho^+\pi^0)$ is also consistent with the previous BESIII result [37] within 1.5σ . We also observe an obvious $D^+ \rightarrow \bar{K}_1(1400)^0(\rightarrow \bar{K}^{*0}\pi^0)\pi^+$ signal, but no $D^+ \rightarrow K_1(1270)^+\pi^0$, where the significance is 3.9σ . This phenomenon is consistent with the theoretical prediction [43] and similar to that in $D^+ \rightarrow K_S^0\pi^+\pi^+\pi^-$, where the FF of $D^+ \rightarrow K_1(1400)\pi$ is about 10 times that of $D^+ \rightarrow K_1(1270)\pi$ [37]. The specific BFs of $D \rightarrow K_1(1270)\pi$ and $D \rightarrow K_1(1400)\pi$ from amplitude analyses can provide inputs to further investigations of the mixing between these two axial-vector kaon mesons [10].

Acknowledgments

The BESIII Collaboration thanks the staff of BEPCII and the IHEP computing center for their strong support. This work is supported in part by National Key R&D Program of China under Contracts Nos. 2020YFA0406400, 2020YFA0406300; National Natural Science Foundation of China (NSFC) under Contracts Nos. 11635010, 11735014, 11835012, 11935015, 11935016, 11935018, 11961141012, 12022510, 12025502, 12035009, 12035013, 12061131003, 12192260, 12192261, 12192262, 12192263, 12192264, 12192265, 12221005, 12225509, 12235017; the Chinese Academy of Sciences (CAS) Large-Scale Scientific Facility Program; the CAS Center for Excellence in Particle Physics (CCEPP); CAS Key Research Program of Frontier Sciences under Contracts Nos. QYZDJ-SSW-SLH003, QYZDJ-

SSW-SLH040; 100 Talents Program of CAS; The Institute of Nuclear and Particle Physics (INPAC) and Shanghai Key Laboratory for Particle Physics and Cosmology; ERC under Contract No. 758462; European Union's Horizon 2020 research and innovation programme under Marie Skłodowska-Curie grant agreement under Contract No. 894790; German Research Foundation DFG under Contracts Nos. 443159800, 455635585, Collaborative Research Center CRC 1044, FOR5327, GRK 2149; Istituto Nazionale di Fisica Nucleare, Italy; Ministry of Development of Turkey under Contract No. DPT2006K-120470; National Research Foundation of Korea under Contract No. NRF-2022R1A2C1092335; National Science and Technology fund of Mongolia; National Science Research and Innovation Fund (NSRF) via the Program Management Unit for Human Resources & Institutional Development, Research and Innovation of Thailand under Contract No. B16F640076; Polish National Science Centre under Contract No. 2019/35/O/ST2/02907; The Swedish Research Council; U. S. Department of Energy under Contract No. DE-FG02-05ER41374

A Two-dimensional fit on $M_{\text{BC}}^{\text{sig}}$ versus $M_{\text{BC}}^{\text{tag}}$

The signal yield of DT candidates is determined by fitting to the 2D $M_{\text{BC}}^{\text{tag}}$ versus $M_{\text{BC}}^{\text{sig}}$ distribution. Signal events with both the tag side and signal side reconstructed correctly should concentrate around $M_{\text{BC}}^{\text{sig}} = M_{\text{BC}}^{\text{tag}} = M_{D^+}$, where M_{D^+} is the known D^+ mass. Besides signal events, we define three kinds of background. Candidates with correctly reconstructed D^+ (or D^-) and incorrectly reconstructed D^- (or D^+) are BKGI, which appear around the lines $M_{\text{BC}}^{\text{sig}}$ or $M_{\text{BC}}^{\text{tag}} = M_{D^+}$. Other candidates appearing around the diagonal are mainly from the $D^0\bar{D}^0$ wrong-combination and the $e^+e^- \rightarrow q\bar{q}$ processes (BKGII). The rest of the flat backgrounds mainly comes from candidates reconstructed incorrectly on both sides (BKGIII). Figure 7 shows the distributions of these PDFs. Here we list the probability density functions for different components in the fit:

- Signal: $s(x, y)$,
- BKGI: $b_1(x) \cdot \text{ARGUS}(y; m_0, c, p) + b_2(y) \cdot \text{ARGUS}(x; m_0, c, p)$,
- BKGII: $\text{ARGUS}((x + y)/\sqrt{2}; m_0, c, p) \cdot g((x - y)/\sqrt{2})$,
- BKGIII: $\text{ARGUS}(x; m_0, c, p) \cdot \text{ARGUS}(y; m_0, c, p)$.

The signal shape $s(x, y)$ is described by the 2D MC-simulated shape convolved with a 2D Gaussian. For BKGI, $b_{1,2}(x, y)$ is described by the one-dimensional (1D) MC-simulated shape convoluted with a Gaussian, $\text{ARGUS}(x, y)$ is the ARGUS function [38]. The parameters of the convoluted Gaussian functions are obtained by a 1D fit to M_{BC} on the signal and tag side respectively, and are fixed in the 2D fit. For BKGII, it is an ARGUS function in the diagonal axis multiplied by a Gaussian in the anti-diagonal axis. For BKGIII, it is an ARGUS function in $M_{\text{BC}}^{\text{sig}}$ multiplied by an ARGUS function in $M_{\text{BC}}^{\text{tag}}$. In the fit, the parameters m_0 and p for the ARGUS function are fixed at 1.8865 GeV and 0.5, respectively.

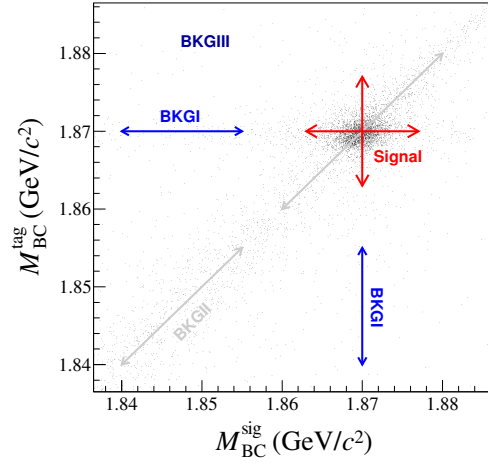


Figure 7. The 2D $M_{\text{BC}}^{\text{tag}}$ versus $M_{\text{BC}}^{\text{sig}}$ distributions for data and different PDFs.

B Other tested intermediate processes

Some other tested amplitudes with significance less than 5σ are listed below. The significance is given in brackets. The resonance $f_0(980)$ only decays to $\pi^0\pi^0$.

- Cascade amplitudes

- $D^+ \rightarrow K_S^0 a_1(1260)^+ [D] (\rightarrow \rho^+ \pi^0) (< 1\sigma)$
- $D^+ \rightarrow K_S^0 a_1(1260)^+ (\rightarrow f_0(980) \pi^+) (3.5\sigma)$
- $D^+ \rightarrow K_1(1270)^+ [S] (\rightarrow K_S^0 \rho^+) \pi^0 (1.7\sigma)$
- $D^+ \rightarrow K_1(1270)^+ [D] (\rightarrow K_S^0 \rho^+) \pi^0 (3.2\sigma)$
- $D^+ \rightarrow K_1(1270)^+ (\rightarrow K_S^0 \rho^+) \pi^0 (3.9\sigma)$
- $D^+ \rightarrow K(1460)^0 (\rightarrow \bar{K}^{*0} \pi^0) \pi^+ (3.3\sigma)$
- $D^+ [D] \rightarrow \bar{K}^{*0} \rho^+ (< 1\sigma)$

- Three-body amplitudes

- $D^+ \rightarrow (K_S^0 \pi^0)_{S-wave} f_0(980) (< 1\sigma)$
- $D^+ \rightarrow (\bar{K}^{*0} \pi^+)_P \pi^0 (3.1\sigma)$
- $D^+ \rightarrow (\bar{K}^{*0} \pi^0)_P \pi^+ (< 1\sigma)$
- $D^+ \rightarrow (K_S^0 \rho^+)_P \pi^0 (< 1\sigma)$
- $D^+ \rightarrow K_S^0 (\rho^+ \pi^0)_A [S] (3.0\sigma)$
- $D^+ \rightarrow K_S^0 (\rho^+ \pi^0)_A [D] (3.6\sigma)$
- $D^+ \rightarrow (\bar{K}^{*0} \pi^0)_A [S] \pi^+ (3.0\sigma)$
- $D^+ \rightarrow (\bar{K}^{*0} \pi^0)_A [D] \pi^+ (< 1\sigma)$
- $D^+ \rightarrow (K_S^0 \rho^+)_A [D] \pi^0 (2.9\sigma)$
- $D^+ \rightarrow (K_S^0 \pi^0)_{S-wave} \rho^+ (4.2\sigma)$
- $D^+ \rightarrow \bar{K}^{*0} (\pi^+ \pi^0)_S (3.2\sigma)$
- $D^+ \rightarrow (\bar{K}^{*0} \pi^0)_V \pi^+ (2.2\sigma)$
- $D^+ \rightarrow K_S^0 (\pi^0 \rho^+)_V (< 1\sigma)$
- $D^+ [S] \rightarrow (K_S^0 \pi^0)_V \rho^+ (3.5\sigma)$
- $D^+ [P] \rightarrow (K_S^0 \pi^0)_V \rho^+ (< 1\sigma)$
- $D^+ [D] \rightarrow (K_S^0 \pi^0)_V \rho^+ (3.4\sigma)$
- $D^+ [P] \rightarrow \bar{K}^{*0} (\pi^+ \pi^0)_V (2.2\sigma)$
- $D^+ [D] \rightarrow \bar{K}^{*0} (\pi^+ \pi^0)_V (< 1\sigma)$

- Four-body non-resonance amplitudes

- $D^+ \rightarrow (K_S^0 \pi^0)_{S-wave} (\pi^+ \pi^0)_S (< 1\sigma)$

- $D^+ \rightarrow (K_S^0 \pi^+)_{S-wave} (\pi^0 \pi^0)_S (< 1\sigma)$
- $D^+ \rightarrow K_S^0 ((\pi^+ \pi^0)_S \pi^0)_A (1.9\sigma)$
- $D^+ \rightarrow K_S^0 ((\pi^0 \pi^0)_S \pi^+)_A (1.6\sigma)$
- $D^+ \rightarrow ((K_S^0 \pi^+)_{S-wave} \pi^0)_A \pi^0 (1.2\sigma)$
- $D^+ \rightarrow ((K_S^0 \pi^0)_{S-wave} \pi^+)_A \pi^0 (1.8\sigma)$
- $D^+ \rightarrow ((K_S^0 \pi^0)_{S-wave} \pi^0)_A \pi^+ (< 1\sigma)$
- $D^+ \rightarrow (K_S^0 (\pi^+ \pi^0)_S)_A \pi^0 (2.1\sigma)$
- $D^+ \rightarrow (K_S^0 (\pi^0 \pi^0)_S)_A \pi^+ (< 1\sigma)$
- $D^+ \rightarrow (K_S^0 \pi^0)_{S-wave} (\pi^+ \pi^0)_V (2.3\sigma)$
- $D^+ \rightarrow (K_S^0 \pi^0)_V (\pi^+ \pi^0)_S (2.2\sigma)$
- $D^+[S] \rightarrow (K_S^0 \pi^0)_V (\pi^+ \pi^0)_V (< 1\sigma)$
- $D^+[P] \rightarrow (K_S^0 \pi^0)_V (\pi^+ \pi^0)_V (2.4\sigma)$
- $D^+[D] \rightarrow (K_S^0 \pi^0)_V (\pi^+ \pi^0)_V (2.0\sigma)$
- $D^+ \rightarrow (K_S^0 \pi^+)_T (\pi^0 \pi^0)_S (2.4\sigma)$
- $D^+ \rightarrow (K_S^0 \pi^0)_T (\pi^+ \pi^0)_S (3.6\sigma)$
- $D^+ \rightarrow (K_S^0 \pi^+)_S (\pi^0 \pi^0)_T (2.1\sigma)$
- $D^+ \rightarrow (K_S^0 \pi^0)_S (\pi^+ \pi^0)_T (1.9\sigma)$

C The interference between processes

The interference between processes, calculated by Eq. (4.31).

	II	III	IV	V	VI	VII	VIII
I	4.88	-1.09	-0.29	15.43	-0.00	-4.39	0.07
II		-1.37	0.05	5.95	0.00	-2.41	0.01
III			-0.22	-9.81	-0.00	7.28	-0.27
IV				1.01	0.00	-0.17	-0.19
V					-0.00	-21.45	9.37
VI						0.00	-0.00
VII							-2.98

Table 8. Interference between processes, in unit of %.

- I $D^+ \rightarrow K_S^0 a_1(1260)^+, a_1(1260)^+[S] \rightarrow \rho^+ \pi^0,$
- II $D^+ \rightarrow K_S^0 a_1(1260)^+, a_1(1260)^+ \rightarrow f_0(500) \pi^+,$
- III $D^+ \rightarrow \bar{K}_1(1400)^0 \pi^+, \bar{K}_1(1400)^0[S] \rightarrow \bar{K}^{*0} \pi^0,$
- IV $D^+ \rightarrow \bar{K}_1(1400)^0 \pi^+, \bar{K}_1(1400)^0[D] \rightarrow \bar{K}^{*0} \pi^0,$
- V $D^+[S] \rightarrow \bar{K}^{*0} \rho^+,$
- VI $D^+[P] \rightarrow \bar{K}^{*0} \rho^+,$
- VII $D^+[S] \rightarrow \bar{K}^{*0} (\pi^+ \pi^0)_V,$
- VIII $D^+ \rightarrow K_S^0 (\rho^+ \pi^0)_P.$

References

- [1] H.-Y. Cheng and C.-W. Chiang, *Two-body hadronic charmed meson decays*, *Phys. Rev. D* **81** (2010) 074021 [[arXiv:1001.0987](#)].
- [2] A. Ryd and A. A. Petrov, *Hadronic D and D_s Meson Decays*, *Rev. Mod. Phys.* **84** (2012) 65 [[arXiv:0910.1265](#)].
- [3] BESIII collaboration, *Measurements of the absolute branching fractions of hadronic D -meson decays involving kaons and pions*, *Phys. Rev. D* **106** (2022) 032002 [[arXiv:2205.14031](#)].
- [4] BESIII collaboration, *Study of the decay $D^+ \rightarrow K^*(892)^+ K_S^0$ in $D^+ \rightarrow K^+ K_S^0 \pi^0$* , *Phys. Rev. D* **104** (2021) 012006 [[arXiv:2104.09131](#)].
- [5] BESIII collaboration, *Amplitude Analysis of the $D^+ \rightarrow K_S^0 \pi^+ \pi^0$ Dalitz Plot*, *Phys. Rev. D* **89** (2014) 052001 [[arXiv:1401.3083](#)].
- [6] FOCUS collaboration, *Dalitz plot analysis of the $D^+ \rightarrow K^- \pi^+ \pi^+$ decay in the FOCUS experiment*, *Phys. Lett. B* **653** (2007) 1 [[arXiv:0705.2248](#)].
- [7] MARK-III collaboration, *Resonant substructure in $\bar{K} \pi \pi$ decays of D mesons*, *Phys. Rev. D* **45** (1992) 2196.
- [8] E. H. E. Aaoud and A. N. Kamal, *Helicity and partial wave amplitude analysis of $D \rightarrow K^* \rho$ decay*, *Phys. Rev. D* **59** (1999) 114013 [[hep-ph/9910350](#)].
- [9] P.-F. Guo, D. Wang and F.-S. Yu, *Strange Axial-vector Mesons in D Meson Decays*, *Nucl. Phys. Rev.* **36** (2019) 125 [[arXiv:1801.09582](#)].
- [10] H.-Y. Cheng, *Revisiting Axial-Vector Meson Mixing*, *Phys. Lett. B* **707** (2012) 116 [[arXiv:1110.2249](#)].
- [11] BESIII collaboration, *Design and construction of the BESIII detector*, *Nucl. Instrum. Meth. A* **614** (2010) 345.
- [12] BESIII collaboration, *Future physics programme of BESIII*, *Chin. Phys. C* **44** (2020) 040001.
- [13] C. Yu et al., *BEPCII Performance and beam dynamics studies on luminosity*, in *Proc. of International Particle Accelerator Conference (IPAC'16), Busan, Korea, May 8-13, 2016*, no. 7 in International Particle Accelerator Conference, (Geneva, Switzerland), pp. 1014–1018, JACoW, June, 2016, [DOI](#).
- [14] MARK-III collaboration, *Direct Measurements of Charmed D Meson Hadronic Branching Fractions*, *Phys. Rev. Lett.* **56** (1986) 2140.
- [15] GEANT4 collaboration, *GEANT4—a simulation toolkit*, *Nucl. Instrum. Meth. A* **506** (2003) 250.
- [16] K.-X. Huang, Z.-J. Li, Z. Qian, J. Zhu, H.-Y. Li, Y.-M. Zhang et al., *Method for detector description transformation to Unity and application in BESIII*, *Nucl. Sci. Tech.* **33** (2022) 142 [[arXiv:2206.10117](#)].
- [17] S. Jadach, B. F. L. Ward and Z. Was, *Coherent exclusive exponentiation for precision Monte Carlo calculations*, *Phys. Rev. D* **63** (2001) 113009.
- [18] S. Jadach, B. F. L. Ward and Z. Was, *The precision Monte Carlo event generator KK for two fermion final states in e^+e^- collisions*, *Comput. Phys. Commun.* **130** (2000) 260.

- [19] D. J. Lange, *The EvtGen particle decay simulation package*, *Nucl. Instrum. Meth. A* **462** (2001) 152.
- [20] R.-G. Ping, *Event generators at BESIII*, *Chin. Phys. C* **32** (2008) 599.
- [21] PARTICLE DATA GROUP collaboration, *Review of Particle Physics*, *PTEP* **2022** (2022) 083C01.
- [22] J. C. Chen, G. S. Huang, X. R. Qi, D. H. Zhang and Y. S. Zhu, *Event generator for J/ψ and $\psi(2S)$ decay*, *Phys. Rev. D* **62** (2000) 034003.
- [23] R.-L. Yang, R.-G. Ping and H. Chen, *Tuning and validation of the Lundcharm model with J/ψ decays*, *Chin. Phys. Lett.* **31** (2014) 061301.
- [24] E. Richter-Was, *QED bremsstrahlung in semileptonic B and leptonic τ decays*, *Phys. Lett. B* **303** (1993) 163 .
- [25] K. Cranmer, *Kernel estimation in high-energy physics*, *Comput. Phys. Commun.* **136** (2001) 198.
- [26] W. Verkerke and D. P. Kirkby, *RooFit users manual v2.91*, *RooFit Users Manual* (2019) .
- [27] BESIII collaboration, *Amplitude analysis and branching fraction measurement of $D_s^+ \rightarrow K^+ K^- \pi^+$* , *Phys. Rev. D* **104** (2021) 012016.
- [28] P. d'Argent, N. Skidmore, J. Benton, J. Dalseno, E. Gersabeck, S. Harnew et al., *Amplitude Analyses of $D^0 \rightarrow \pi^+ \pi^- \pi^+ \pi^-$ and $D^0 \rightarrow K^+ K^- \pi^+ \pi^-$ Decays*, *JHEP* **05** (2017) 143 [[arXiv:1703.08505](#)].
- [29] G. J. Gounaris and J. J. Sakurai, *Finite width corrections to the vector meson dominance prediction for $\rho \rightarrow e^+ e^-$* , *Phys. Rev. Lett.* **21** (1968) 244.
- [30] BES collaboration, *Resonances in $J/\psi \rightarrow \phi \pi^+ \pi^-$ and $\phi K^+ K^-$* , *Phys. Lett. B* **607** (2005) 243.
- [31] D. Bugg, A. Sarantsev and B. Zou, *New results on $\pi\pi$ phase shifts between 600 and 1900 MeV*, *Nucl. Phys. B* **471** (1996) 59.
- [32] J. R. Pelaez, *From controversy to precision on the sigma meson: a review on the status of the non-ordinary $f_0(500)$ resonance*, *Phys. Rept.* **658** (2016) 1.
- [33] D. Aston et al., *A study of $K^- \pi^+$ scattering in the reaction $K^- p \rightarrow K^- \pi^+ n$ at 11 GeV/c*, *Nucl. Phys. B* **296** (1988) 493.
- [34] BABAR, BELLE collaboration, *Measurement of $\cos 2\beta$ in $B^0 \rightarrow D^{(*)} h^0$ with $D \rightarrow K_S^0 \pi^+ \pi^-$ decays by a combined time-dependent Dalitz plot analysis of BABAR and Belle data*, *Phys. Rev. D* **98** (2018) 112012 [[arXiv:1804.06153](#)].
- [35] B. S. Zou and D. V. Bugg, *Covariant tensor formalism for partial-wave analyses of ψ decay to mesons*, *Eur. Phys. J. A* **16** (2003) 537.
- [36] BESIII collaboration, *Amplitude analysis of $D^0 \rightarrow K^- \pi^+ \pi^+ \pi^-$* , *Phys. Rev. D* **95** (2017) 072010 [[arXiv:1701.08591](#)].
- [37] BESIII collaboration, *Amplitude analysis of $D^+ \rightarrow K_S^0 \pi^+ \pi^+ \pi^-$* , *Phys. Rev. D* **100** (2019) 072008 [[arXiv:1901.05936](#)].
- [38] ARGUS collaboration, *Search for Hadronic $b \rightarrow u$ Decays*, *Phys. Lett. B* **241** (1990) 278.
- [39] BESIII collaboration, *Improved measurement of the absolute branching fraction of $D^+ \rightarrow \bar{K}^0 \mu^+ \nu_\mu$* , *Eur. Phys. J. C* **76** (2016) 369 [[arXiv:1605.00068](#)].

- [40] BESIII collaboration, *Measurement of the absolute branching fraction of $D^+ \rightarrow \bar{K}^0 e^+ \nu_e$ via $\bar{K}^0 \rightarrow \pi^0 \pi^0$* , *Chin. Phys. C* **40** (2016) 113001 [[arXiv:1605.00208](#)].
- [41] BESIII collaboration, *Measurement of the branching fraction for the semi-leptonic decay $D^{0(+)} \rightarrow \pi^{-(0)} \mu^+ \nu_\mu$ and test of lepton universality*, *Phys. Rev. Lett.* **121** (2018) 171803 [[arXiv:1802.05492](#)].
- [42] BESIII collaboration, *Study of decay dynamics and CP asymmetry in $D^+ \rightarrow K_L^0 e^+ \nu_e$ decay*, *Phys. Rev. D* **92** (2015) 112008 [[arXiv:1510.00308](#)].
- [43] H.-Y. Cheng, *Hadronic charmed meson decays involving axial vector mesons*, *Phys. Rev. D* **67** (2003) 094007 [[hep-ph/0301198](#)].

The BESIII Collaboration

M. Ablikim¹, M. N. Achasov^{5,b}, P. Adlarson⁷⁵, X. C. Ai⁸¹, R. Aliberti³⁶, A. Amoroso^{74A,74C}, M. R. An⁴⁰, Q. An^{71,58}, Y. Bai⁵⁷, O. Bakina³⁷, I. Balossino^{30A}, Y. Ban^{47,g}, V. Batozskaya^{1,45}, K. Begzsuren³³, N. Berger³⁶, M. Berlowski⁴⁵, M. Bertani^{29A}, D. Bettoni^{30A}, F. Bianchi^{74A,74C}, E. Bianco^{74A,74C}, A. Bortone^{74A,74C}, I. Boyko³⁷, R. A. Briere⁶, A. Brueggemann⁶⁸, H. Cai⁷⁶, X. Cai^{1,58}, A. Calcaterra^{29A}, G. F. Cao^{1,63}, N. Cao^{1,63}, S. A. Cetin^{62A}, J. F. Chang^{1,58}, T. T. Chang⁷⁷, W. L. Chang^{1,63}, G. R. Che⁴⁴, G. Chelkov^{37,a}, C. Chen⁴⁴, Chao Chen⁵⁵, G. Chen¹, H. S. Chen^{1,63}, M. L. Chen^{1,58,63}, S. J. Chen⁴³, S. M. Chen⁶¹, T. Chen^{1,63}, X. R. Chen^{32,63}, X. T. Chen^{1,63}, Y. B. Chen^{1,58}, Y. Q. Chen³⁵, Z. J. Chen^{26,h}, W. S. Cheng^{74C}, S. K. Choi^{11A}, X. Chu⁴⁴, G. Cibinetto^{30A}, S. C. Coen⁴, F. Cossio^{74C}, J. J. Cui⁵⁰, H. L. Dai^{1,58}, J. P. Dai⁷⁹, A. Dbeyssi¹⁹, R. E. de Boer⁴, D. Dedovich³⁷, Z. Y. Deng¹, A. Denig³⁶, I. Denysenko³⁷, M. Destefanis^{74A,74C}, F. De Mori^{74A,74C}, B. Ding^{66,1}, X. X. Ding^{47,g}, Y. Ding⁴¹, Y. Ding³⁵, J. Dong^{1,58}, L. Y. Dong^{1,63}, M. Y. Dong^{1,58,63}, X. Dong⁷⁶, M. C. Du¹, S. X. Du⁸¹, Z. H. Duan⁴³, P. Egorov^{37,a}, Y. L. Fan⁷⁶, J. Fang^{1,58}, S. S. Fang^{1,63}, W. X. Fang¹, Y. Fang¹, R. Farinelli^{30A}, L. Fava^{74B,74C}, F. Feldbauer⁴, G. Felici^{29A}, C. Q. Feng^{71,58}, J. H. Feng⁵⁹, K. Fischer⁶⁹, M. Fritsch⁴, C. Fritsch⁶⁸, C. D. Fu¹, J. L. Fu⁶³, Y. W. Fu¹, H. Gao⁶³, Y. N. Gao^{47,g}, Yang Gao^{71,58}, S. Garbolino^{74C}, I. Garzia^{30A,30B}, P. T. Ge⁷⁶, Z. W. Ge⁴³, C. Geng⁵⁹, E. M. Gersabeck⁶⁷, A. Gilman⁶⁹, K. Goetzen¹⁴, L. Gong⁴¹, W. X. Gong^{1,58}, W. Grad³⁶, S. Gramigna^{30A,30B}, M. Greco^{74A,74C}, M. H. Gu^{1,58}, Y. T. Gu¹⁶, C. Y. Guan^{1,63}, Z. L. Guan²³, A. Q. Guo^{32,63}, L. B. Guo⁴², M. J. Guo⁵⁰, R. P. Guo⁴⁹, Y. P. Guo^{13,f}, A. Guskov^{37,a}, T. T. Han⁵⁰, W. Y. Han⁴⁰, X. Q. Hao²⁰, F. A. Harris⁶⁵, K. K. He⁵⁵, K. L. He^{1,63}, F. H. Heinsius⁴, C. H. Heinz³⁶, Y. K. Heng^{1,58,63}, C. Herold⁶⁰, T. Holtmann⁴, P. C. Hong^{13,f}, G. Y. Hou^{1,63}, X. T. Hou^{1,63}, Y. R. Hou⁶³, Z. L. Hou¹, H. M. Hu^{1,63}, J. F. Hu^{56,i}, T. Hu^{1,58,63}, Y. Hu¹, G. S. Huang^{71,58}, K. X. Huang⁵⁹, L. Q. Huang^{32,63}, X. T. Huang⁵⁰, Y. P. Huang¹, T. Hussain⁷³, N. Hüsken^{28,36}, W. Imoehl²⁸, M. Irshad^{71,58}, J. Jackson²⁸, S. Jaeger⁴, S. Janchiv³³, J. H. Jeong^{11A}, Q. Ji¹, Q. P. Ji²⁰, X. B. Ji^{1,63}, X. L. Ji^{1,58}, Y. Y. Ji⁵⁰, X. Q. Jia⁵⁰, Z. K. Jia^{71,58}, H. J. Jiang⁷⁶, P. C. Jiang^{47,g}, S. S. Jiang⁴⁰, T. J. Jiang¹⁷, X. S. Jiang^{1,58,63}, Y. Jiang⁶³, J. B. Jiao⁵⁰, Z. Jiao²⁴, S. Jin⁴³, Y. Jin⁶⁶, M. Q. Jing^{1,63}, T. Johansson⁷⁵, X. K.¹, S. Kabana³⁴, N. Kalantar-Nayestanaki⁶⁴, X. L. Kang¹⁰, X. S. Kang⁴¹, R. Kappert⁶⁴, M. Kavatsyuk⁶⁴, B. C. Ke⁸¹, A. Khoukaz⁶⁸, R. Kiuchi¹, R. Kliemt¹⁴, O. B. Kolcu^{62A}, B. Kopf⁴, M. K. Kuessner⁴, A. Kupsc^{45,75}, W. Kühn³⁸, J. J. Lane⁶⁷, P. Larin¹⁹, A. Lavania²⁷, L. Lavezzi^{74A,74C}, T. T. Lei^{71,k}, Z. H. Lei^{71,58}, H. Leithoff³⁶, M. Lellmann³⁶, T. Lenz³⁶, C. Li⁴⁴, C. Li⁴⁸, C. H. Li⁴⁰, Cheng Li^{71,58}, D. M. Li⁸¹, F. Li^{1,58}, G. Li¹, H. Li^{71,58}, H. B. Li^{1,63}, H. J. Li²⁰, H. N. Li^{56,i}, Hui Li⁴⁴, J. R. Li⁶¹, J. S. Li⁵⁹, J. W. Li⁵⁰, K. L. Li²⁰, Ke Li¹, L. J Li^{1,63}, L. K. Li¹, Lei Li³, M. H. Li⁴⁴, P. R. Li^{39,j,k}, Q. X. Li⁵⁰, S. X. Li¹³, T. Li⁵⁰, W. D. Li^{1,63}, W. G. Li¹, X. H. Li^{71,58}, X. L. Li⁵⁰, Xiaoyu Li^{1,63}, Y. G. Li^{47,g}, Z. J. Li⁵⁹, Z. X. Li¹⁶, C. Liang⁴³, H. Liang³⁵, H. Liang^{1,63}, H. Liang^{71,58}, Y. F. Liang⁵⁴, Y. T. Liang^{32,63}, G. R. Liao¹⁵, L. Z. Liao⁵⁰, Y. P. Liao^{1,63}, J. Libby²⁷, A. Limphirat⁶⁰, D. X. Lin^{32,63}, T. Lin¹, B. J. Liu¹, B. X. Liu⁷⁶, C. Liu³⁵, C. X. Liu¹, F. H. Liu⁵³, Fang Liu¹, Feng Liu⁷, G. M. Liu^{56,i}, H. Liu^{39,j,k}, H. B. Liu¹⁶, H. M. Liu^{1,63}, Huanhuan Liu¹, Huihui Liu²², J. B. Liu^{71,58}, J. L. Liu⁷², J. Y. Liu^{1,63}, K. Liu¹, K. Y. Liu⁴¹, Ke Liu²³, L. Liu^{71,58}, L. C. Liu⁴⁴, Lu Liu⁴⁴, M. H. Liu^{13,f}, P. L. Liu¹, Q. Liu⁶³,

S. B. Liu^{71,58}, T. Liu^{13,f}, W. K. Liu⁴⁴, W. M. Liu^{71,58}, X. Liu^{39,j,k}, Y. Liu^{39,j,k}, Y. Liu⁸¹,
 Y. B. Liu⁴⁴, Z. A. Liu^{1,58,63}, Z. Q. Liu⁵⁰, X. C. Lou^{1,58,63}, F. X. Lu⁵⁹, H. J. Lu²⁴, J. G. Lu^{1,58},
 X. L. Lu¹, Y. Lu⁸, Y. P. Lu^{1,58}, Z. H. Lu^{1,63}, C. L. Luo⁴², M. X. Luo⁸⁰, T. Luo^{13,f},
 X. L. Luo^{1,58}, X. R. Lyu⁶³, Y. F. Lyu⁴⁴, F. C. Ma⁴¹, H. L. Ma¹, J. L. Ma^{1,63}, L. L. Ma⁵⁰,
 M. M. Ma^{1,63}, Q. M. Ma¹, R. Q. Ma^{1,63}, R. T. Ma⁶³, X. Y. Ma^{1,58}, Y. Ma^{47,g}, Y. M. Ma³²,
 F. E. Maas¹⁹, M. Maggiora^{74A,74C}, S. Malde⁶⁹, Q. A. Malik⁷³, A. Mangoni^{29B}, Y. J. Mao^{47,g},
 Z. P. Mao¹, S. Marcello^{74A,74C}, Z. X. Meng⁶⁶, J. G. Messchendorp^{14,64}, G. Mezzadri^{30A},
 H. Miao^{1,63}, T. J. Min⁴³, R. E. Mitchell²⁸, X. H. Mo^{1,58,63}, N. Yu. Muchnoi^{5,b}, Y. Nefedov³⁷,
 F. Nerling^{19,d}, I. B. Nikolaev^{5,b}, Z. Ning^{1,58}, S. Nisar^{12,l}, Y. Niu⁵⁰, S. L. Olsen⁶³, Q. Ouyang^{1,58,63},
 S. Pacetti^{29B,29C}, X. Pan⁵⁵, Y. Pan⁵⁷, A. Pathak³⁵, P. Patteri^{29A}, Y. P. Pei^{71,58}, M. Pelizaeus⁴,
 H. P. Peng^{71,58}, K. Peters^{14,d}, J. L. Ping⁴², R. G. Ping^{1,63}, S. Plura³⁶, S. Pogodin³⁷,
 V. Prasad³⁴, F. Z. Qi¹, H. Qi^{71,58}, H. R. Qi⁶¹, M. Qi⁴³, T. Y. Qi^{13,f}, S. Qian^{1,58}, W. B. Qian⁶³,
 C. F. Qiao⁶³, J. J. Qin⁷², L. Q. Qin¹⁵, X. P. Qin^{13,f}, X. S. Qin⁵⁰, Z. H. Qin^{1,58}, J. F. Qiu¹,
 S. Q. Qu⁶¹, C. F. Redmer³⁶, K. J. Ren⁴⁰, A. Rivetti^{74C}, V. Rodin⁶⁴, M. Rolo^{74C}, G. Rong^{1,63},
 Ch. Rosner¹⁹, S. N. Ruan⁴⁴, N. Salone⁴⁵, A. Sarantsev^{37,c}, Y. Schelhaas³⁶, K. Schoenning⁷⁵,
 M. Scodeggio^{30A,30B}, K. Y. Shan^{13,f}, W. Shan²⁵, X. Y. Shan^{71,58}, J. F. Shangguan⁵⁵,
 L. G. Shao^{1,63}, M. Shao^{71,58}, C. P. Shen^{13,f}, H. F. Shen^{1,63}, W. H. Shen⁶³, X. Y. Shen^{1,63},
 B. A. Shi⁶³, H. C. Shi^{71,58}, J. L. Shi¹³, J. Y. Shi¹, Q. Q. Shi⁵⁵, R. S. Shi^{1,63}, X. Shi^{1,58},
 J. J. Song²⁰, T. Z. Song⁵⁹, W. M. Song^{35,1}, Y. J. Song¹³, Y. X. Song^{47,g}, S. Sosio^{74A,74C},
 S. Spataro^{74A,74C}, F. Stieler³⁶, Y. J. Su⁶³, G. B. Sun⁷⁶, G. X. Sun¹, H. Sun⁶³, H. K. Sun¹,
 J. F. Sun²⁰, K. Sun⁶¹, L. Sun⁷⁶, S. S. Sun^{1,63}, T. Sun^{1,63}, W. Y. Sun³⁵, Y. Sun¹⁰, Y. J. Sun^{71,58},
 Y. Z. Sun¹, Z. T. Sun⁵⁰, Y. X. Tan^{71,58}, C. J. Tang⁵⁴, G. Y. Tang¹, J. Tang⁵⁹, Y. A. Tang⁷⁶,
 L. Y. Tao⁷², Q. T. Tao^{26,h}, M. Tat⁶⁹, J. X. Teng^{71,58}, V. Thoren⁷⁵, W. H. Tian⁵⁹, W. H. Tian⁵²,
 Y. Tian^{32,63}, Z. F. Tian⁷⁶, I. Uman^{62B}, S. J. Wang⁵⁰, B. Wang¹, B. L. Wang⁶³, Bo Wang^{71,58},
 C. W. Wang⁴³, D. Y. Wang^{47,g}, F. Wang⁷², H. J. Wang^{39,j,k}, H. P. Wang^{1,63}, J. P. Wang⁵⁰,
 K. Wang^{1,58}, L. L. Wang¹, M. Wang⁵⁰, Meng Wang^{1,63}, S. Wang^{39,j,k}, S. Wang^{13,f},
 T. Wang^{13,f}, T. J. Wang⁴⁴, W. Wang⁷², W. Wang⁵⁹, W. P. Wang^{71,58}, X. Wang^{47,g},
 X. F. Wang^{39,j,k}, X. J. Wang⁴⁰, X. L. Wang^{13,f}, Y. Wang⁶¹, Y. D. Wang⁴⁶, Y. F. Wang^{1,58,63},
 Y. H. Wang⁴⁸, Y. N. Wang⁴⁶, Y. Q. Wang¹, Yaqian Wang^{18,1}, Yi Wang⁶¹, Z. Wang^{1,58}, Z. L.
 Wang⁷², Z. Y. Wang^{1,63}, Ziyi Wang⁶³, D. Wei⁷⁰, D. H. Wei¹⁵, F. Weidner⁶⁸, S. P. Wen¹,
 C. W. Wenzel⁴, U. W. Wiedner⁴, G. Wilkinson⁶⁹, M. Wolke⁷⁵, L. Wollenberg⁴, C. Wu⁴⁰,
 J. F. Wu^{1,63}, L. H. Wu¹, L. J. Wu^{1,63}, X. Wu^{13,f}, X. H. Wu³⁵, Y. Wu⁷¹, Y. J. Wu³²,
 Z. Wu^{1,58}, L. Xia^{71,58}, X. M. Xian⁴⁰, T. Xiang^{47,g}, D. Xiao^{39,j,k}, G. Y. Xiao⁴³, H. Xiao^{13,f},
 S. Y. Xiao¹, Y. L. Xiao^{13,f}, Z. J. Xiao⁴², C. Xie⁴³, X. H. Xie^{47,g}, Y. Xie⁵⁰, Y. G. Xie^{1,58},
 Y. H. Xie⁷, Z. P. Xie^{71,58}, T. Y. Xing^{1,63}, C. F. Xu^{1,63}, C. J. Xu⁵⁹, G. F. Xu¹, H. Y. Xu⁶⁶,
 Q. J. Xu¹⁷, Q. N. Xu³¹, W. Xu^{1,63}, W. L. Xu⁶⁶, X. P. Xu⁵⁵, Y. C. Xu⁷⁸, Z. P. Xu⁴³,
 Z. S. Xu⁶³, F. Yan^{13,f}, L. Yan^{13,f}, W. B. Yan^{71,58}, W. C. Yan⁸¹, X. Q. Yan¹, H. J. Yang^{51,e},
 H. L. Yang³⁵, H. X. Yang¹, Tao Yang¹, Y. Yang^{13,f}, Y. F. Yang⁴⁴, Y. X. Yang^{1,63}, Yi-
 fan Yang^{1,63}, Z. W. Yang^{39,j,k}, Z. P. Yao⁵⁰, M. Ye^{1,58}, M. H. Ye⁹, J. H. Yin¹, Z. Y. You⁵⁹,
 B. X. Yu^{1,58,63}, C. X. Yu⁴⁴, G. Yu^{1,63}, J. S. Yu^{26,h}, T. Yu⁷², X. D. Yu^{47,g}, C. Z. Yuan^{1,63},
 L. Yuan², S. C. Yuan¹, X. Q. Yuan¹, Y. Yuan^{1,63}, Z. Y. Yuan⁵⁹, C. X. Yue⁴⁰, A. A. Zafar⁷³,
 F. R. Zeng⁵⁰, X. Zeng^{13,f}, Y. Zeng^{26,h}, Y. J. Zeng^{1,63}, X. Y. Zhai³⁵, Y. C. Zhai⁵⁰, Y. H. Zhan⁵⁹,
 A. Q. Zhang^{1,63}, B. L. Zhang^{1,63}, B. X. Zhang¹, D. H. Zhang⁴⁴, G. Y. Zhang²⁰, H. Zhang⁷¹,

H. H. Zhang⁵⁹, H. H. Zhang³⁵, H. Q. Zhang^{1,58,63}, H. Y. Zhang^{1,58}, J. J. Zhang⁵², J. L. Zhang²¹, J. Q. Zhang⁴², J. W. Zhang^{1,58,63}, J. X. Zhang^{39,j,k}, J. Y. Zhang¹, J. Z. Zhang^{1,63}, Jianyu Zhang⁶³, Jiawei Zhang^{1,63}, L. M. Zhang⁶¹, L. Q. Zhang⁵⁹, Lei Zhang⁴³, P. Zhang¹, Q. Y. Zhang^{40,81}, Shuihan Zhang^{1,63}, Shulei Zhang^{26,h}, X. D. Zhang⁴⁶, X. M. Zhang¹, X. Y. Zhang⁵⁰, Xuyan Zhang⁵⁵, Y. Zhang⁷², Y. Zhang⁶⁹, Y. T. Zhang⁸¹, Y. H. Zhang^{1,58}, Yan Zhang^{71,58}, Yao Zhang¹, Z. H. Zhang¹, Z. L. Zhang³⁵, Z. Y. Zhang⁴⁴, Z. Y. Zhang⁷⁶, G. Zhao¹, J. Zhao⁴⁰, J. Y. Zhao^{1,63}, J. Z. Zhao^{1,58}, Lei Zhao^{71,58}, Ling Zhao¹, M. G. Zhao⁴⁴, S. J. Zhao⁸¹, Y. B. Zhao^{1,58}, Y. X. Zhao^{32,63}, Z. G. Zhao^{71,58}, A. Zhemchugov^{37,a}, B. Zheng⁷², J. P. Zheng^{1,58}, W. J. Zheng^{1,63}, Y. H. Zheng⁶³, B. Zhong⁴², X. Zhong⁵⁹, H. Zhou⁵⁰, L. P. Zhou^{1,63}, X. Zhou⁷⁶, X. K. Zhou⁷, X. R. Zhou^{71,58}, X. Y. Zhou⁴⁰, Y. Z. Zhou^{13,f}, J. Zhu⁴⁴, K. Zhu¹, K. J. Zhu^{1,58,63}, L. Zhu³⁵, L. X. Zhu⁶³, S. H. Zhu⁷⁰, S. Q. Zhu⁴³, T. J. Zhu^{13,f}, W. J. Zhu^{13,f}, Y. C. Zhu^{71,58}, Z. A. Zhu^{1,63}, J. H. Zou¹, J. Zu^{71,58}

¹ *Institute of High Energy Physics, Beijing 100049, People's Republic of China*

² *Beihang University, Beijing 100191, People's Republic of China*

³ *Beijing Institute of Petrochemical Technology, Beijing 102617, People's Republic of China*

⁴ *Bochum Ruhr-University, D-44780 Bochum, Germany*

⁵ *Budker Institute of Nuclear Physics SB RAS (BINP), Novosibirsk 630090, Russia*

⁶ *Carnegie Mellon University, Pittsburgh, Pennsylvania 15213, USA*

⁷ *Central China Normal University, Wuhan 430079, People's Republic of China*

⁸ *Central South University, Changsha 410083, People's Republic of China*

⁹ *China Center of Advanced Science and Technology, Beijing 100190, People's Republic of China*

¹⁰ *China University of Geosciences, Wuhan 430074, People's Republic of China*

¹¹ *Chung-Ang University, Seoul, 06974, Republic of Korea*

¹² *COMSATS University Islamabad, Lahore Campus, Defence Road, Off Raiwind Road, 54000 Lahore, Pakistan*

¹³ *Fudan University, Shanghai 200433, People's Republic of China*

¹⁴ *GSI Helmholtzcentre for Heavy Ion Research GmbH, D-64291 Darmstadt, Germany*

¹⁵ *Guangxi Normal University, Guilin 541004, People's Republic of China*

¹⁶ *Guangxi University, Nanning 530004, People's Republic of China*

¹⁷ *Hangzhou Normal University, Hangzhou 310036, People's Republic of China*

¹⁸ *Hebei University, Baoding 071002, People's Republic of China*

¹⁹ *Helmholtz Institute Mainz, Staudinger Weg 18, D-55099 Mainz, Germany*

²⁰ *Henan Normal University, Xinxiang 453007, People's Republic of China*

²¹ *Henan University, Kaifeng 475004, People's Republic of China*

²² *Henan University of Science and Technology, Luoyang 471003, People's Republic of China*

²³ *Henan University of Technology, Zhengzhou 450001, People's Republic of China*

²⁴ *Huangshan College, Huangshan 245000, People's Republic of China*

²⁵ *Hunan Normal University, Changsha 410081, People's Republic of China*

²⁶ *Hunan University, Changsha 410082, People's Republic of China*

- ²⁷ *Indian Institute of Technology Madras, Chennai 600036, India*
- ²⁸ *Indiana University, Bloomington, Indiana 47405, USA*
- ²⁹ *INFN Laboratori Nazionali di Frascati, (A)INFN Laboratori Nazionali di Frascati, I-00044, Frascati, Italy; (B)INFN Sezione di Perugia, I-06100, Perugia, Italy; (C)University of Perugia, I-06100, Perugia, Italy*
- ³⁰ *INFN Sezione di Ferrara, (A)INFN Sezione di Ferrara, I-44122, Ferrara, Italy; (B)University of Ferrara, I-44122, Ferrara, Italy*
- ³¹ *Inner Mongolia University, Hohhot 010021, People's Republic of China*
- ³² *Institute of Modern Physics, Lanzhou 730000, People's Republic of China*
- ³³ *Institute of Physics and Technology, Peace Avenue 54B, Ulaanbaatar 13330, Mongolia*
- ³⁴ *Instituto de Alta Investigación, Universidad de Tarapacá, Casilla 7D, Arica 1000000, Chile*
- ³⁵ *Jilin University, Changchun 130012, People's Republic of China*
- ³⁶ *Johannes Gutenberg University of Mainz, Johann-Joachim-Becher-Weg 45, D-55099 Mainz, Germany*
- ³⁷ *Joint Institute for Nuclear Research, 141980 Dubna, Moscow region, Russia*
- ³⁸ *Justus-Liebig-Universität Giessen, II. Physikalisches Institut, Heinrich-Buff-Ring 16, D-35392 Giessen, Germany*
- ³⁹ *Lanzhou University, Lanzhou 730000, People's Republic of China*
- ⁴⁰ *Liaoning Normal University, Dalian 116029, People's Republic of China*
- ⁴¹ *Liaoning University, Shenyang 110036, People's Republic of China*
- ⁴² *Nanjing Normal University, Nanjing 210023, People's Republic of China*
- ⁴³ *Nanjing University, Nanjing 210093, People's Republic of China*
- ⁴⁴ *Nankai University, Tianjin 300071, People's Republic of China*
- ⁴⁵ *National Centre for Nuclear Research, Warsaw 02-093, Poland*
- ⁴⁶ *North China Electric Power University, Beijing 102206, People's Republic of China*
- ⁴⁷ *Peking University, Beijing 100871, People's Republic of China*
- ⁴⁸ *Qufu Normal University, Qufu 273165, People's Republic of China*
- ⁴⁹ *Shandong Normal University, Jinan 250014, People's Republic of China*
- ⁵⁰ *Shandong University, Jinan 250100, People's Republic of China*
- ⁵¹ *Shanghai Jiao Tong University, Shanghai 200240, People's Republic of China*
- ⁵² *Shanxi Normal University, Linfen 041004, People's Republic of China*
- ⁵³ *Shanxi University, Taiyuan 030006, People's Republic of China*
- ⁵⁴ *Sichuan University, Chengdu 610064, People's Republic of China*
- ⁵⁵ *Soochow University, Suzhou 215006, People's Republic of China*
- ⁵⁶ *South China Normal University, Guangzhou 510006, People's Republic of China*
- ⁵⁷ *Southeast University, Nanjing 211100, People's Republic of China*
- ⁵⁸ *State Key Laboratory of Particle Detection and Electronics, Beijing 100049, Hefei 230026, People's Republic of China*
- ⁵⁹ *Sun Yat-Sen University, Guangzhou 510275, People's Republic of China*
- ⁶⁰ *Suranaree University of Technology, University Avenue 111, Nakhon Ratchasima 30000, Thailand*
- ⁶¹ *Tsinghua University, Beijing 100084, People's Republic of China*

- ⁶² Turkish Accelerator Center Particle Factory Group, (A)Istinye University, 34010, Istanbul, Turkey; (B)Near East University, Nicosia, North Cyprus, 99138, Mersin 10, Turkey
- ⁶³ University of Chinese Academy of Sciences, Beijing 100049, People's Republic of China
- ⁶⁴ University of Groningen, NL-9747 AA Groningen, The Netherlands
- ⁶⁵ University of Hawaii, Honolulu, Hawaii 96822, USA
- ⁶⁶ University of Jinan, Jinan 250022, People's Republic of China
- ⁶⁷ University of Manchester, Oxford Road, Manchester, M13 9PL, United Kingdom
- ⁶⁸ University of Muenster, Wilhelm-Klemm-Strasse 9, 48149 Muenster, Germany
- ⁶⁹ University of Oxford, Keble Road, Oxford OX13RH, United Kingdom
- ⁷⁰ University of Science and Technology Liaoning, Anshan 114051, People's Republic of China
- ⁷¹ University of Science and Technology of China, Hefei 230026, People's Republic of China
- ⁷² University of South China, Hengyang 421001, People's Republic of China
- ⁷³ University of the Punjab, Lahore-54590, Pakistan
- ⁷⁴ University of Turin and INFN, (A)University of Turin, I-10125, Turin, Italy; (B)University of Eastern Piedmont, I-15121, Alessandria, Italy; (C)INFN, I-10125, Turin, Italy
- ⁷⁵ Uppsala University, Box 516, SE-75120 Uppsala, Sweden
- ⁷⁶ Wuhan University, Wuhan 430072, People's Republic of China
- ⁷⁷ Xinyang Normal University, Xinyang 464000, People's Republic of China
- ⁷⁸ Yantai University, Yantai 264005, People's Republic of China
- ⁷⁹ Yunnan University, Kunming 650500, People's Republic of China
- ⁸⁰ Zhejiang University, Hangzhou 310027, People's Republic of China
- ⁸¹ Zhengzhou University, Zhengzhou 450001, People's Republic of China

^a Also at the Moscow Institute of Physics and Technology, Moscow 141700, Russia

^b Also at the Novosibirsk State University, Novosibirsk, 630090, Russia

^c Also at the NRC "Kurchatov Institute", PNPI, 188300, Gatchina, Russia

^d Also at Goethe University Frankfurt, 60323 Frankfurt am Main, Germany

^e Also at Key Laboratory for Particle Physics, Astrophysics and Cosmology, Ministry of Education; Shanghai Key Laboratory for Particle Physics and Cosmology; Institute of Nuclear and Particle Physics, Shanghai 200240, People's Republic of China

^f Also at Key Laboratory of Nuclear Physics and Ion-beam Application (MOE) and Institute of Modern Physics, Fudan University, Shanghai 200443, People's Republic of China

^g Also at State Key Laboratory of Nuclear Physics and Technology, Peking University, Beijing 100871, People's Republic of China

^h Also at School of Physics and Electronics, Hunan University, Changsha 410082, China

ⁱ Also at Guangdong Provincial Key Laboratory of Nuclear Science, Institute of Quantum Matter, South China Normal University, Guangzhou 510006, China

^j Also at Frontiers Science Center for Rare Isotopes, Lanzhou University, Lanzhou 730000, People's Republic of China

^k Also at Lanzhou Center for Theoretical Physics, Lanzhou University, Lanzhou 730000, People's Republic of China

^l Also at the Department of Mathematical Sciences, IBA, Karachi 75270, Pakistan